Titre: Title:	Automatic Classification of Closed Angle Glaucoma in Anterior Eye Segment Images
Auteur: Author:	Doha Zrouki
Date:	2025
Type:	Mémoire ou thèse / Dissertation or Thesis
Référence: Citation:	Zrouki, D. (2025). Automatic Classification of Closed Angle Glaucoma in Anterior Eye Segment Images [Mémoire de maîtrise, Polytechnique Montréal]. PolyPublie. https://publications.polymtl.ca/62679/

URL de PolyPublie: PolyPublie URL:	https://publications.polymtl.ca/62679/
Directeurs de recherche: Advisors:	Lama Séoud
Programme: Program:	Génie Informatique

POLYTECHNIQUE MONTRÉAL
affiliée à l'Université de Montréal

Automatic classification of closed angle glaucoma in anterior eye segment images

DOHA ZROUKI
Département de génie informatique et génie logiciel

Mémoire présenté en vue de l'obtention du diplôme de *Maîtrise ès sciences appliquées*
Génie informatique

Janvier 2025

POLYTECHNIQUE MONTRÉAL
affiliée à l'Université de Montréal

Ce mémoire intitulé :

Automatic classification of closed angle glaucoma in anterior eye segment images

présenté par **Doha ZROUKI**
en vue de l'obtention du diplôme de *Maîtrise ès sciences appliquées*
a été dûment accepté par le jury d'examen constitué de :

Farida CHERIET, présidente
Lama SÉOUD, membre et directrice de recherche
Sébastien GAGNÉ, membre externe

ACKNOWLEDGEMENTS

I would first like to thank my research supervisor, Lama Séoud, without whom I would never have completed this master's degree. Thank you for your exceptional supervision, your cheerfulness, your availability and your dedication to your students.

I'd also like to thank my colleagues, who helped me a lot when I was stuck, especially Philippe Baumstimer and Victor Nogues. Thank you both so much!

I'd also like to thank my parents for their support and encouragement, and my brother for all the times he came to pick me up very, very late at Poly while I was writing this thesis. Thanks to Ihsane for feeding and caffeinating me during this period too.

RÉSUMÉ

Le glaucome primaire à angle fermé est une des principales causes de cécité dans le monde, particulièrement répandu chez les populations âgées et certains groupes ethniques. La détection précoce est essentielle pour prévenir la perte de vision irréversible. Cependant, les méthodes diagnostiques classiques, telles que la tomographie par cohérence optique (OCT), la gonioscopie et la tonométrie, sont souvent coûteuses, nécessitent un équipement spécialisé ou provoquent un inconfort pour les patients. Cette recherche propose l'exploration d'une alternative non invasive basée sur le test de Van Herick, qui évalue l'angle de la chambre antérieure à partir d'images externes de l'œil, sans contact direct avec l'œil ni de dilatation pupillaire par l'usage de gouttes mydriatiques.

L'objectif de travail est de développer un processus automatisé d'aide au diagnostic utilisant des techniques classiques de traitement d'images pour calculer le ratio de Van Herick, un indicateur clé du risque de du glaucome à angle-fermé. Le jeu de données a été enrichi par l'acquisition de nouvelles images de segments antérieurs pour compléter les bases existantes. L'algorithme segmente et analyse les réflexions des fentes lumineuses dans les images du segment antérieur de l'oeil et calcule les mesures nécessaires, validées par des annotations cliniques fournies par un ophtalmologiste. Les résultats, évalués à l'aide de métriques telles que la sensibilité, la spécificité, le score F1 et la courbe ROC, montrent des performances prometteuses, notamment pour les classifications regroupant les cas modérés et sévères.

Ce travail met en évidence le potentiel des techniques classiques de traitement d'images pour la détection efficace et évolutive du risque de glaucome à angle fermé, en particulier dans les régions isolées ou à ressources limitées, en permettant un dépistage automatisé et non invasif.

ABSTRACT

Primary Angle Closure Glaucoma (PACG) is a leading cause of blindness worldwide, particularly prevalent among aging populations and certain ethnic groups. Early detection is essential to prevent irreversible vision loss, but traditional diagnostic methods such as Optical Coherence Tomography (OCT), gonioscopy, and tonometry are often costly, require specialized equipment, and cause patient discomfort. This research proposes an alternative approach based on the Van Herick test, which uses external eye images to assess the anterior chamber angle non-invasively, avoiding direct eye contact or pupil dilation.

The study develops an automated diagnostic pipeline utilizing classical image processing techniques to calculate the Van Herick ratio, a key indicator of PACG risk. The dataset was enhanced by acquiring new anterior segment images to complement existing databases. The pipeline segments and analyzes light slit reflections in the images and computes the necessary measurements, validated against clinical annotations provided by ophthalmologists. Performance metrics such as recall, precision, F1 score, and ROC curve, demonstrate promising results, especially for grouped classifications of moderate and severe cases.

This work demonstrates the potential of using classical image processing techniques for the efficient and scalable detection of PACG, particularly in remote or resource-constrained environments. By enabling automated and non-invasive screening.

TABLE OF CONTENTS

LIST OF TABLES

LIST OF FIGURES

LIST OF SYMBOLS AND ACRONYMS

PACG	Primary Angle Closure Glaucoma
RGCs	Retinal Ganglion Cells
PLR	Pupillary Light Reflex
AH	Aqueous Humor
IOP	Intraocular Pressure
PC	Posterior Chamber
AC	Anterior Chamber
TM	Trabecular Meshwork
ITC	Iridotrabecular Contact
PAS	Peripheral Anterior Synechiae
OCT	Optical Coherence Tomography
CDR	Cup-to-disc ratio
CDA	Cup-to-disc area ratio
RNFL	Retinal Nerve Fiber Layer
ACD	Anterior Chamber Depth
AS-OCT	Anterior segment optical coherence tomography
AUC	Area under the curve
ROI	Region Of Interest
CCA	Connected Component Analysis

LIST OF APPENDICES

CHAPTER 1 INTRODUCTION

The eye is a highly sensitive and vital organ for vision and overall quality of life. Numerous ocular diseases progress silently, often with no noticeable symptoms [7], leading to severe and sometimes irreversible consequences. Access to ophthalmological care, however, is not always available or convenient. A significant portion of the population lacks access to regular eye examinations due to a shortage of specialists and inadequate healthcare services [8]. In Canada, only 40% of the population aged between 19 and 64 y.o. visited an eye care professional in 2015 [9]. Regular ocular exams are crucial to diagnose pathologies in their early stages and avoid severe and irreversible medical consequences such as vision impairment [10].

Our partner, LightX Innovations, is developing a tele-ophthalmology platform that integrates a stereoscopic imaging system for the anterior segment of the eye and machine learning algorithms, aiming to digitize the conventional slit-lamp exam. Their long-term vision is to enhance accessibility to ophthalmological care by enabling remote consultations with ophthalmologists, thereby addressing barriers faced by individuals in rural or underserved areas. By facilitating early detection of glaucoma and other ocular diseases, they ultimately aspire to transform the delivery of eye care and promote equitable health outcomes.

Glaucoma is an umbrella term for a group of eye diseases that lead to irreversible vision loss by damaging the optic nerve and retinal ganglion cells [11]. Glaucoma is classified into two main categories, primary glaucoma when there is no underlying medical condition, and secondary glaucoma when it is caused by a known medical condition [12].

Glaucoma is the second leading cause of blindness in the world [13] with 80 million people suffering from it globally [14]. There are several factors that significantly increase the risk of developing glaucoma. These include diabetes, family history, gender, age, and ethnic origin. Diabetes doubles the risk of glaucoma [13]. As for ethnic origin, studies show that black individuals are 6 to 8 times more at risk of being diagnosed with glaucoma than caucasians [13]. Additionally, a review of ethnicity and continents reveals that the highest prevalence of primary angle closure glaucoma (PACG) is found in Asia (0.73%) [15]. Primary angle closure glaucoma is also more prevalent in women than in men, with a risk ratio of 0.7% [15]. Furthermore, people above the age of 80 years have the highest risk with a prevalence of 2.8% [15].

This project focuses exclusively on primary angle closure glaucoma (PACG). Also known as acute or narrow-angle glaucoma, PACG is considered a medical emergency due to its rapid progression [16]. Early detection is crucial to prevent irreversible vision loss, making it a

priority for the development of an automatic diagnostic method.

Conventional ways to diagnose glaucoma include tonometry, ophthalmoscopy, gonioscopy, and OCT (Optical Coherence Tomography). Tonometry is used to measure intraocular pressure by applying force on the eye's surface, often needing anesthetic drops to numb the area, which may cause discomfort to patients. Ophthalmoscopy involves examining the optic nerve through dilated pupils, requiring the use of mydriatic drops and a skilled professional. These dilating drops can affect vision for 4 to 8 hours, and in some cases, the effect can last up to 24 hours [17]. Gonioscopy utilizes a lens to examine the eyes drainage angle and requires direct contact with the eye and specialized expertise. OCT provides high-resolution cross-sectional images of the retina, allowing for detailed analysis of the optic nerve and retinal layers. However the equipment is expensive and is not easily accessible in resource constrained settings.

This project investigates the potential of external eye images acquired using LightX's smartphone mounted slit-lamp device for detecting signs of primary angle closure glaucoma. Images of the anterior segment of the eye are captured using cameras mounted on a slit lamp. This setup allows for eight tests to be performed, but for the purpose of this work, we only focus on images from the Van Herick test. This test is used to evaluate the anterior chamber (AC) angle of the eye by assessing the ratio of the peripheral anterior chamber depth to the corneal thickness [18]. Visually, the Van Herick test involves a slit lamp equipped with a narrow vertical beam of light that is directed across the cornea. This beam projects a shadow of the anterior chamber angle, which is then compared to the thickness of the cornea. The resulting image provides the depth of the AC and the angle formed between the cornea and the iris. A narrow anterior chamber can indicate a higher risk for closed-angle glaucoma.

Currently, a trained ophthalmologist evaluates the Van Herick images to derive, at a glance, a classification of the PACG's degree. It is prone to observer variability, tedious and time-consuming. Thus, the goal of this project is to propose and evaluate an automatic quantification of the ratio from the Van Herick images.

This non-invasive approach is particularly valuable for diagnosing closed-angle glaucoma as it does not involve direct contact with the eye, as opposed to gonioscopy [19], making it more comfortable for patients. Furthermore, it is more cost-effective [19] than alternative imaging techniques such as Optical Coherence Tomography (OCT), and does not necessitate pupil dilation or a highly trained operator. These attributes significantly improve its accessibility across diverse clinical environments, including resource-limited and rural settings.

This thesis is organized as follows. Chapter 2 provides background knowledge on the eye anatomy, glaucoma and specifically closed-angle glaucoma, and a review of the relevant

literature. Chapter 3 outlines the rationale and objectives of the project. Chapter 4 details the methodology, including the data collection process and the proposed image processing pipeline. Chapter 5 presents and discusses the results, before concluding with the project's limitations and suggesting directions for future work in Chapter 6.

CHAPTER 2 LITERATURE REVIEW

This chapter covers basic concepts that are important for understanding the thesis, with the anatomy of the eye, the description of glaucoma and available imaging modalities for its diagnosis. It also provides a literature review on methods for computational analysis of eye images.

2.1 Eye anatomy

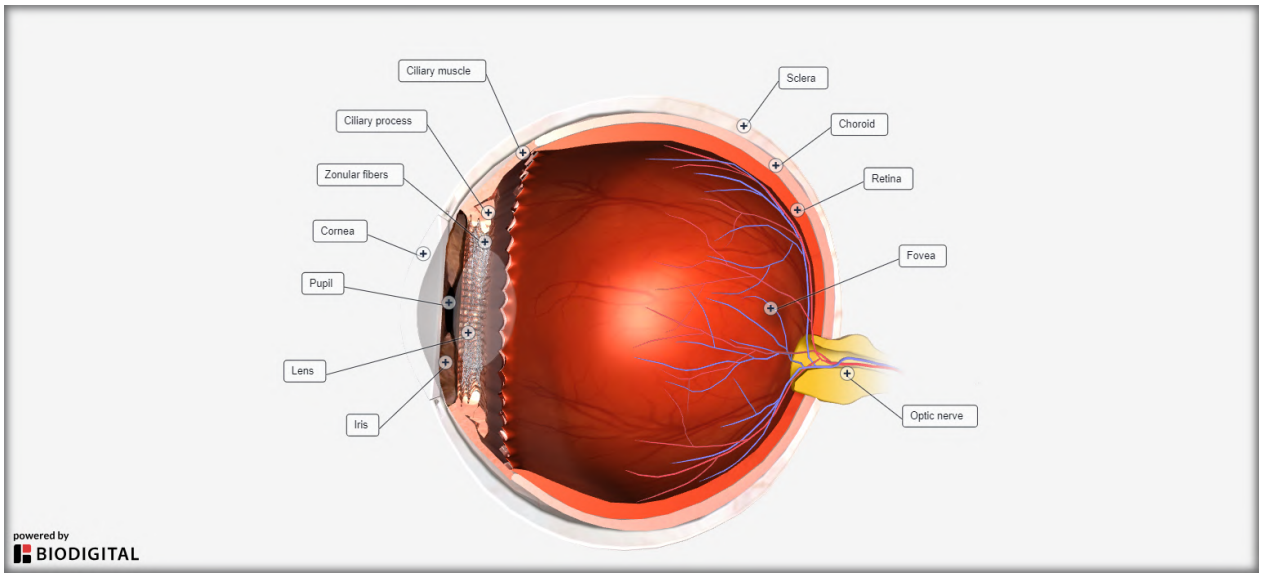

Figure 2.1 Cross-section eye anatomy [1]

The eye is made up of an intricate set of tissues that guide light to the retina.

The anterior segment of the eye corresponds to the front part of the eye (figure 2.1 and the left part of figure 2.2), including the cornea, the iris, the pupil, the lens, the ciliary body, part of the sclera and the anterior chamber (AC), filled with a fluid called the aqueous humor.

The cornea is a transparent bowl-shaped structure at the front of the eye that covers the iris and pupil, which is the entrance point of light towards the lens. The iris controls the amount of light entering the eye by dilating and contracting, adjusting the size of the light aperture, which plays an essential role in environmental adaptation and night vision. The lens focuses light on the retina, insuring optimal vision [20].

The aqueous humor (AH) is a liquid made by epithelial cells in the ciliary body. Its main

function is supplying the non-vascularized tissues of the eye, lens and cornea with nutrients and oxygen [21]. Additionally, the alkaline AH helps to eliminate debris and waste from the different eye tissues, as well as maintaining the eye shape by providing a constant intraocular pressure (IOP) [21]. The AH is produced at a rate of 2 to 3 μl/min [21]. IOP is maintained through the balance of AH production and elimination rates. After its formation by the epithelial cells, the aqueous humor flows from the posterior chamber (PC) to the anterior chamber (AC) through the pupil and is drained using three different routes. The majority drains from the PC to the AC through the trabecular meshwork (TM) into the Schlemm canal (figure 2.2). This route is dependent on the IOP [22]. 20% of the AH drains though the uveoscleral pathway, passing through the suprachoroidal space and the ciliary muscles, this pathway is also IOP-dependent. The third is responsible for a negligible amount of AH outflow, a small quantity of fluid drains directly through the iris into the anterior chamber [22]. The normal range of IOP is between 10 mmHg and 21 mm Hg [22] [23] and can vary during the day. In the morning the IOP is expected to be higher than by the end of the day [22]. An IOP higher than 21 is a risk indicator of glaucoma but not a diagnostic tool. Some individuals with high intraocular pressure never develop glaucoma.

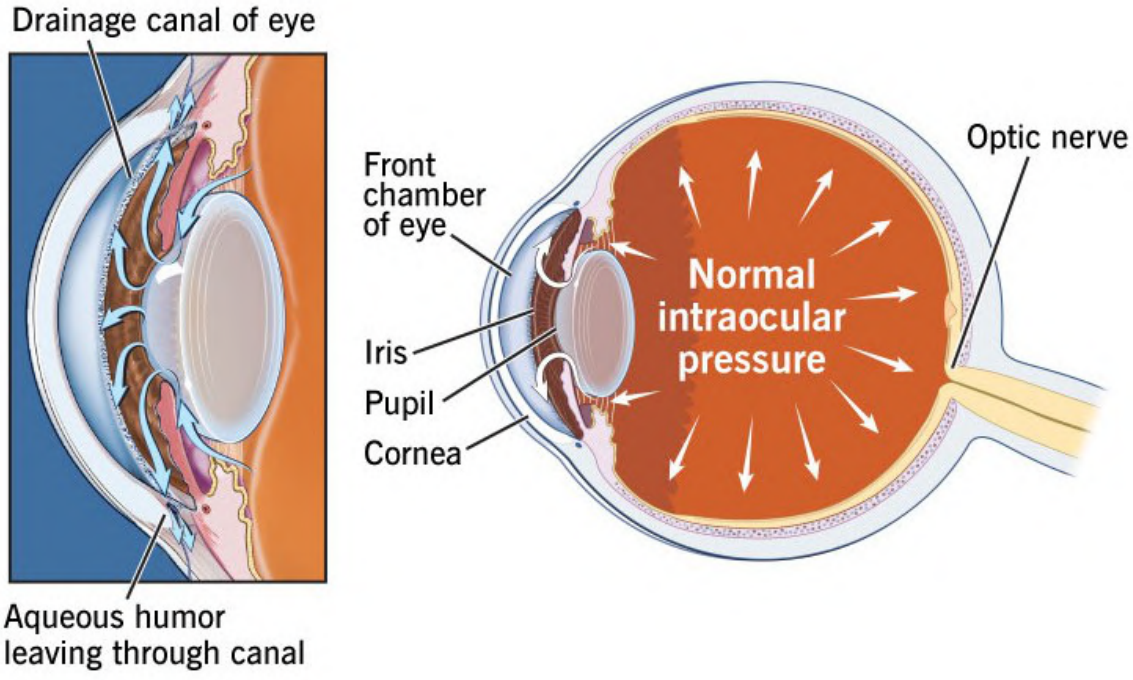

Figure 2.2 Healthy Eye [2]

The posterior segment is the back of the ocular globe, including the retina, the optic nerve, the fovea and the posterior chamber, filled with the vitreous humor [20].

The inner layer of the retina is lined with specialized cells. The retinal ganglion cells (RGCs) possess long axons that converge to form the optic nerve and extend into the brain, transmitting visual information. On average, each retina contains approximately 1.2 to 1.5 million RGCs [24], with each RGC receiving input from around 100 **rods and cones**. **Rods** are photoreceptor cells distributed mainly at the retina's periphery. They play a crucial role in peripheral vision and are essential for low-light or night vision, with about 125 million rods per retina [25]. **Cones**, responsible for color vision, come in three types: S-cones (blue), M-cones (green), and L-cones (red) [26] (figure 2.3). Unlike rods, cones are concentrated primarily in the fovea (figure 2.1). While most RGCs support visual function, a subset regulates **circadian rhythm**s and the **pupillary light reflex** [24]. **Circadian rhythms** act as the body's internal 24-hour clock, governing sleep-wake cycles, hormone release, and other physiological processes [27]. These light-sensitive RGCs send signals to the brain to help regulate these rhythms in response to external light cues. Meanwhile, **the pupillary light reflex (PLR)** automatically adjusts the eye's response to varying light conditions by activating the iris muscles, modifying the pupil size to allow more photons in low-light conditions, and less photons in the opposite scenario [28], ensuring proper adaptation in different environments.

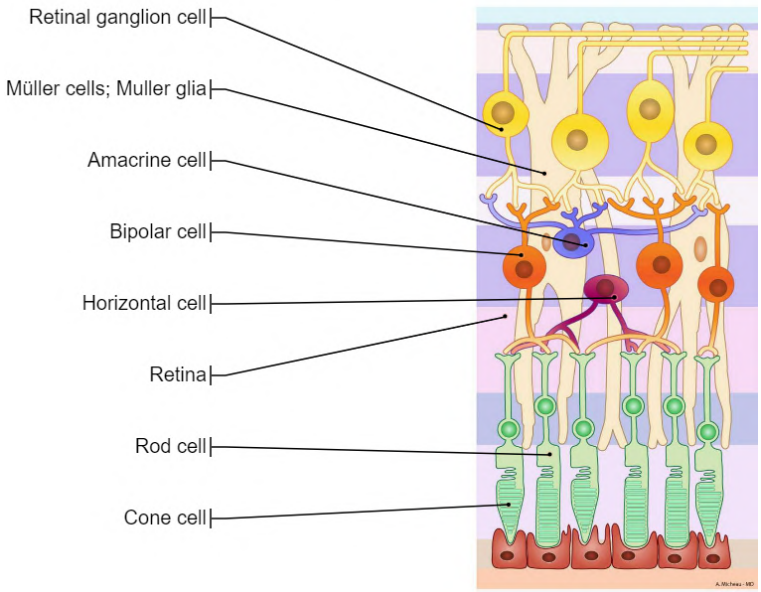

Figure 2.3 Retinal Ganglion Cells (RGCs), Rods and Cones [3]

2.2 Glaucoma

Glaucoma is a group of eye conditions that can lead to blindness, primarily characterized by thinning of the retinal nerve fiber layer [29], progressive excavation of the optic disc [29] and the progressive loss of retinal ganglion cells (RGCs) [16] [29].

There are two main categories of glaucoma based on its underlying cause: primary and secondary. Primary glaucoma occurs when no identifiable cause is found, while secondary glaucoma is associated with an underlying medical condition [12]. Another categorization for glaucoma is according to the configuration of the AC angle. Open-angle glaucoma is when the AC angle is wide, while closed-angle glaucoma is when the AC angle is narrow and closed, affecting AH outflow (figure 2.4).

Primary glaucoma includes several subtypes, such as open-angle glaucoma, the most common form, which is characterized by pressure buildup within the eye [12]. Another subtype is normal-tension glaucoma, a form of open-angle glaucoma where optic nerve damage occurs without elevated intraocular pressure. Angle-closure glaucoma, also referred to as narrow-angle or acute glaucoma, is a medical emergency that requires immediate attention [12], it is more detailed in Section 2.3. Additionally, congenital glaucoma is a rare form present from birth.

Secondary glaucoma encompasses forms of the disease linked to specific conditions. For instance, neovascular glaucoma results from diabetes or high blood pressure [12], while pigmentary glaucoma is caused by pigment dispersion within the eye. Exfoliation glaucoma occurs due to the accumulation of extracellular material on the lens and other structures, and uveitic glaucoma is associated with intraocular inflammation [12].

2.3 Primary Angle Closure Glaucoma

Closed-angle glaucoma is characterized by the closure of the anterior chamber angle. This condition is mainly caused by a build-up of fluid in the posterior chamber, which increases the pressure relative to the anterior chamber. The aqueous humor that flows from the posterior chamber is blocked at the pupil, causing bowing of the iris and resulting in a narrowing of the angle between the iris and cornea [30], that can lead to iridotrabecular contact (ITC), which is the contact between the iris and the anterior chamber angle [31].

Although a disturbance of the homeostasis of AH flow is a direct cause for PACG, the exact mechanism responsible for increasing IOP is not fully understood [22]. Inflammation of eye tissues are one of the causes of IOP fluctuations. For example, an inflammation of the

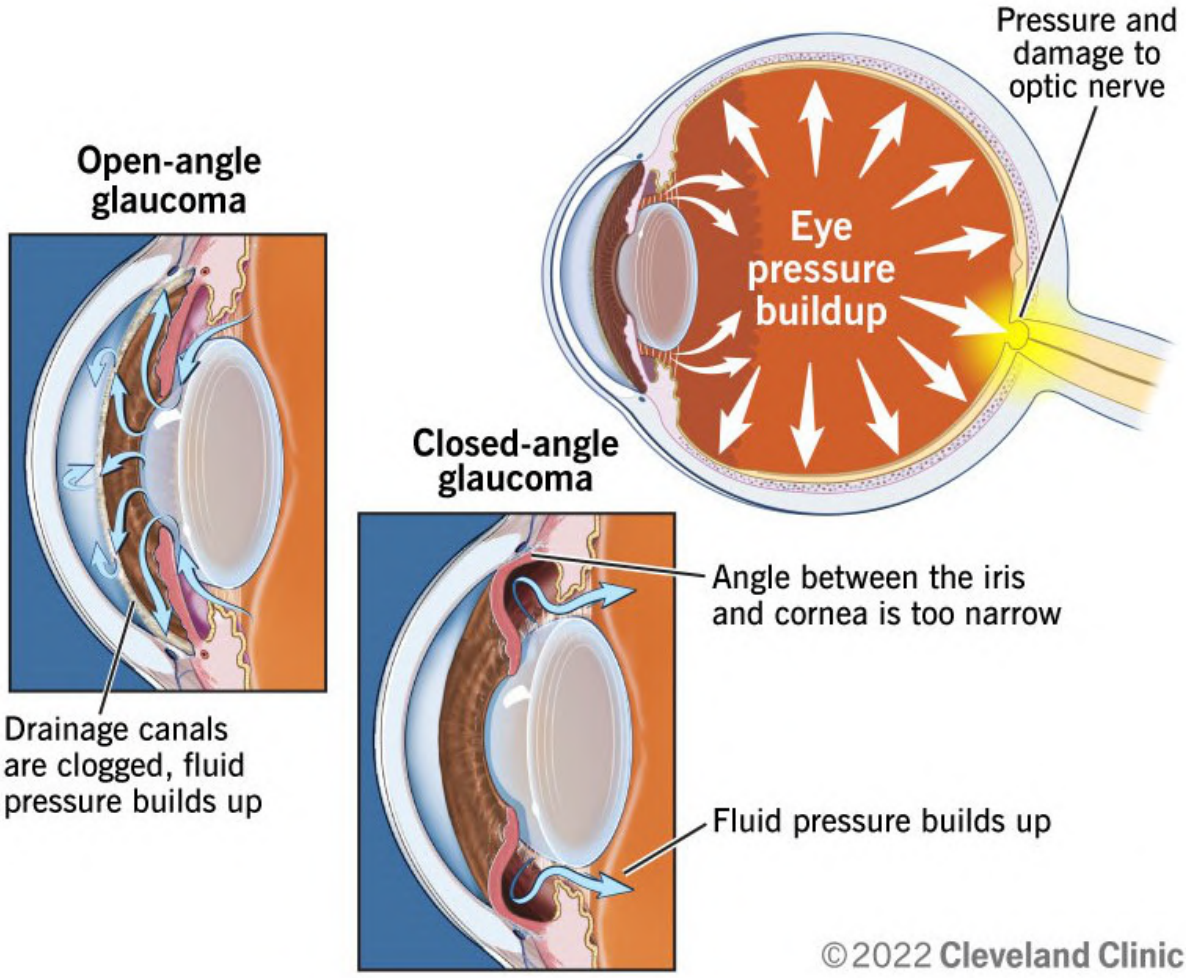

Figure 2.4 Glaucomatous eye [2]

anterior uveal tract disturbs the AH outflow, hence increasing the IOP. Another example is the inflammation of the pars plicata of the ciliary body that produces the AH, which can result in a lower production rate, thus lowering the IOP [22]. For PACG, a high intraocular pressure for a prolonged period leads to permanent damage.

Acute PACG is considered an emergency and requires immediate medical intervention to prevent further damage and blindness. Some possible symptoms are ocular radiating pain, conjunctival hyperemia (dilatation of the blood vessels in the conjunctiva, causing the sclera to appear red), headache, nausea and a sensation of a firm, rigid eye [29] [31]. However, in most cases, PACG is chronic, meaning that the IOP gradually increases with no symptoms [32].

2.4 Clinical diagnosis

There are two types of diagnoses in PACG screening: PACG-suspect patients and PACG-confirmed patients. The former requires regular follow-ups and additional testing. Individuals are considered PACG suspects if gonioscopy shows iridotrabecular contact (ITC) without elevated intraocular pressure (IOP), optic nerve damage, or peripheral anterior synechiae (PAS) [31], the latter occurring when the iris adheres to the angle [33]. In contrast, a confirmed PACG diagnosis requires observed ITC during gonioscopy with either elevated IOP (measured by tonometry) or PAS. Optic nerve damage can result from the progression of PACG but is not a diagnostic criterion.

The first step in PACG screening is clinical history, the patient is asked about previous ocular symptoms, family history, other health concerns and systemic medications, since some drugs can cause ciliary body edema (swelling) [31].

The next steps involve a physical examination, which includes various tests such as refractive status assessment, pupil examination, slit-lamp or biomicroscopic examination, ophthalmoscopy [34], tonometry [35] [34], gonioscopy, optical coherence tomography (OCT) [35] and visual field test or perimetry [35] [34]. These tests are presented in the following subsections.

Assessing the patient's refractive status is also crucial. For example, individuals with hyperopia tend to have shorter axial lengths, resulting in a narrower anterior chamber (AC) angle, which is a known risk factor for PACG [31].

2.4.1 Slit-lamp and Van Herick

A slit lamp focuses a narrow, adjustable beam of light to provide a detailed, stereoscopic view of the eyelids, conjunctiva, cornea, anterior chamber, iris, lens, and anterior vitreous [36]. It is used to detect corneal abnormalities (such as foreign bodies, abrasions), measure anterior chamber depth, identify anterior chamber cells and protein (Tyndall effect), evaluate cataract severity, and diagnose conditions like macular degeneration, diabetic retinopathy, and retinal tears [36]. The Van Herick technique (See 2.5), performed using the slit lamp, estimates the depth of the anterior chamber angle and is particularly useful for identifying narrow angles, a significant risk factor for PACG. If patients are suspected of PACG, this test is followed by tonometry to measure the IOP, gonioscopy to confirm the diagnosis, perimetry and OCT to evaluate the damage to the optic nerve [31].
The Van Herick test is performed using a narrow slit, projected at the limbus (junction of the cornea and the sclera) with an angle of 60° [4] [37]. The distance between the projected slit and its reflection on the iris is proportional to the AC angle. The standard measure

associated with this test is the Van Herick score. It corresponds to the ratio between the width of the empty space between the projected slit and its reflection, and the width of the projected slit. The angle has 4 possible grading values, from 1/4 to 4/4, the smaller ratio corresponds to very narrow angles (figure 2.5).

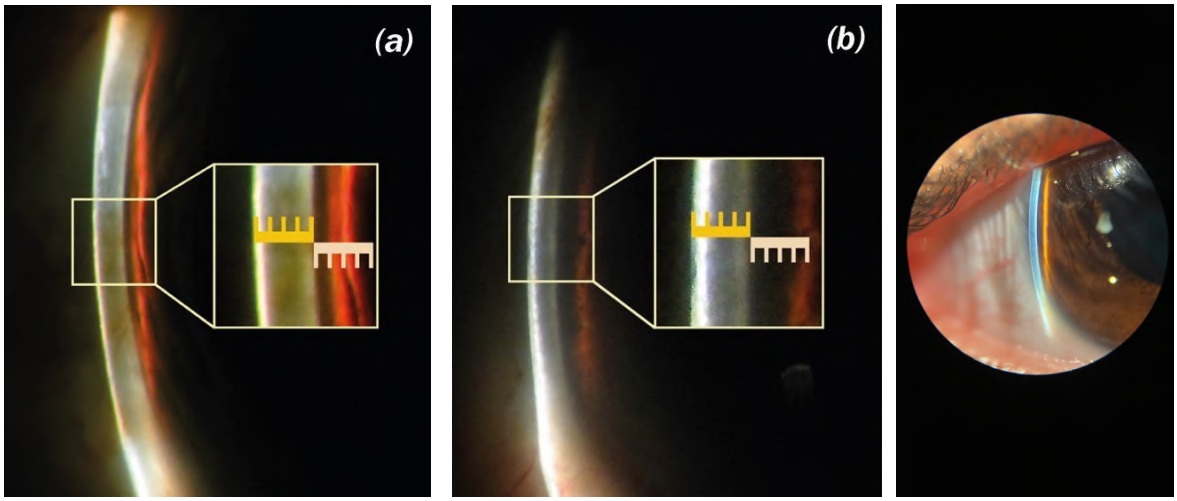

(a) Narrow Angle (b) Open Angle (c) Sample Image

Figure 2.5 Van Herick score: The ratio between the thickness of the projected slit on the cornea (yellow) and the empty space between the slit and its reflection on the iris (white) is correlated to the anterior chamber depth [4].

2.4.2 Tonometry

Tonometry is used to measure intraocular pressure (IOP), a critical parameter in PACG management, as it represents the sole risk factor that can be actively controlled [29] [35]. Additionally, it provides a quantitative measure that is systematically monitored during follow-up visits to evaluate disease progression and treatment outcomes [38]. Intraocular pressure (IOP) can be measured using various techniques, including applanation tonometry, indentation tonometry, rebound tonometry, and dynamic contour tonometry [23]. Tonometry is performed using an applanation tonometer, which involves the application of local anesthetic and fluorescein drops to ensure patient comfort and facilitate measurement [5] [39]. The slit lamp is equipped with a blue filter to enhance visualization of the fluorescein. The tonometer head, or the prism, is gently advanced toward the cornea until contact is made at the center of the cornea (figure 2.6). The process continues until the cornea is flattened, and the force required to achieve this is directly proportional to the intraocular pressure. While most methods involve direct contact with the cornea, a non-contact applanation tonome-

ter—commonly known as the air-puff tonometer—uses a burst of air to flatten the cornea. This approach eliminates the need for anesthetic or fluorescein drops, making it more comfortable for patients. However, the air-puff tonometer is less accurate and less sensitive compared to the Goldmann applanation tonometer [39], which remains the gold standard for IOP [23].

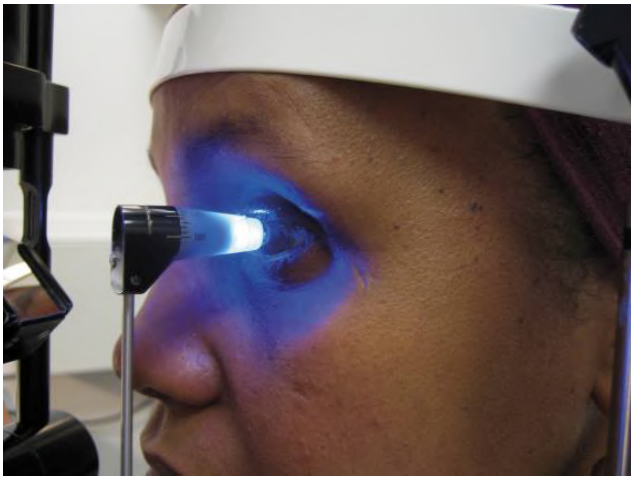

Figure 2.6 Goldmann Applanatation Tonometer [5]

2.4.3 Gonioscopy

Gonioscopy is a diagnostic procedure performed using a specialized lens, known as a gonioscope, which is placed in direct contact with the cornea. To ensure patient comfort, numbing eye drops are applied beforehand [40]. This examination allows ophthalmologists to evaluate the iridocorneal angle—the area where the iris and cornea meet—essential for assessing the eye's drainage system. In cases of PACG, gonioscopy helps determine the extent of the angle closure, playing an essential role in diagnosis [41] [40]. This technique is the standard for confirming PACG and requires advanced clinical expertise [42] [43].

2.4.4 Ophtalmoscopy

An ophthalmoscope is a non-invasive instrument used to examine the fundus, part of the posterior segment of the eye. By directing a beam of light through the pupil, it enables visualization of structures such as the optic disc and the optic nerve, which are essential for assessing structural changes associated with primary angle-closure glaucoma (PACG). PACG is characterized by damage to the optic nerve fibers, leading to visible changes in the

optic disc [44], such as an enlarged optic cup, disc hemorrhages, and a pale optic disc (figure 2.7) [6]. To better visualize the fundus, mydriatic drops are often used to dilate the pupil, causing lasting discomfort. However the AC depth needs to be assessed before dilation to avoid triggering an acute angle-closure glaucoma attack [36].

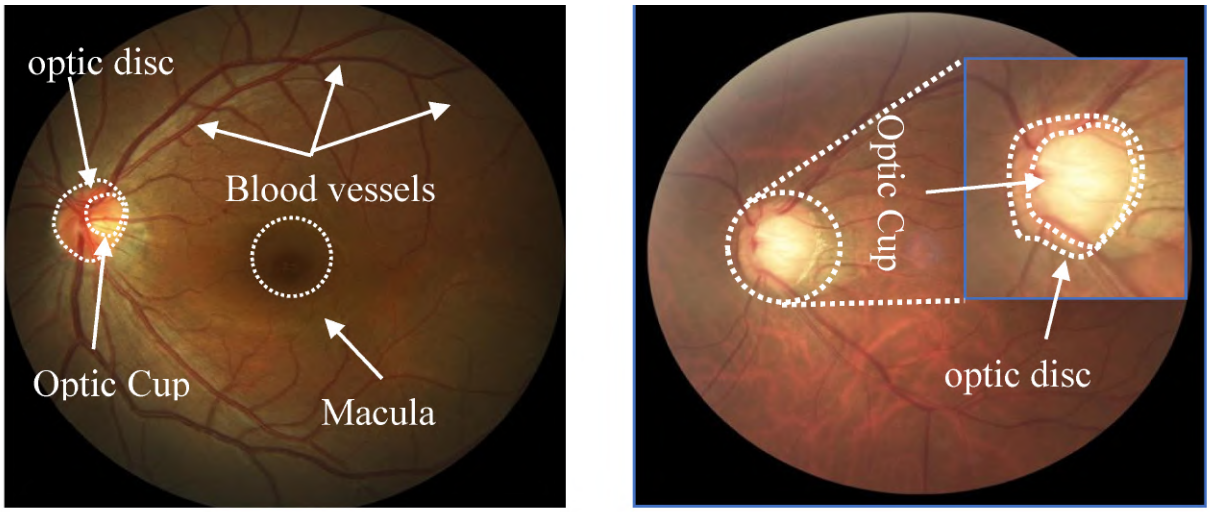

Figure 2.7 Fundus images (ophtalmoscopy) of normal (left) and glaucomatous (right) eyes. [6]

The optic nerve region consists of two components: the optic disc and the optic cup. The optic cup is the brighter, central portion within the optic disc where nerve fibers converge to form the optic nerve as it exits the retina. In healthy eyes, the optic cup is relatively small compared to the optic disc. However, damage to the optic nerve fibers, as seen in glaucoma, reduces the number of nerve fibers, causing "cupping", or enlargement of the optic cup relative to the optic disc, which is a sign of glaucoma [45]. The cup-to-disc ratio (CDR) quantifies the relative size of the optic cup to the optic disc and is a key metric for evaluating glaucoma severity and progression. An increased CDR typically indicates significant optic nerve damage and disease progression [46].

The cup-to-disc ratio (CDR) is calculated by dividing the vertical diameter of the optic cup by the vertical diameter of the optic disc. Another metric used in glaucoma assessment is the cup-to-disc area ratio (CDA), which is the proportion of the optic cup area to the total optic disc area. Both metrics are commonly employed in the characterization of glaucoma [46].

2.4.5 Optical Coherence Tomography (OCT)

Optical Coherence Tomography (OCT) in ophthalmology is an advanced imaging technique that uses low-coherence near-infrared light [45] to produce high-resolution cross-sectional images of the retinal tissue layers, enabling precise assessment of glaucoma progression [47]. One of the earliest detectable signs of glaucoma is the thinning of the retinal nerve fiber layer (RNFL) [45] [47], which can be accurately measured using OCT [47]. This high-resolution imaging allows clinicians to quantify structural changes in the retina and monitor the progression of glaucomatous damage over time. Additionally, OCT provides detailed measurements of the optic nerve head, including the cup-to-disc ratio [47], a critical parameter for assessing the extent of optic nerve damage and evaluating glaucoma severity (as explained in section 2.4.4). By facilitating the early detection and tracking of structural changes, OCT plays an essential role in the diagnosis and management of glaucoma. This high resolution imagery technique comes at hight costs and is not easily available in resource-constrained environments [48].

2.4.6 Perimetry

Perimetry is a diagnostic test used to quantify the visual field of the eye. There are different types of visual field exams, such as : confrontation visual field test, automated static perimetry test, kinetic visual field test, frequency doubling perimetry, eletroretinography, and Amsler grid [49]. The most specific and complete test is the automated static perimetry test, it provides a detailed map of the patient's visual range [49]. During the test, the patient fixates on a central target while small light stimuli are presented at different locations within the visual field [50]. The patient indicates detection of the stimuli by pressing a button, and the results are compiled into a topographic representation of the visual field. This exam is particularly important in glaucoma assessment as it can detect early deterioration in peripheral vision, which is often the first visual deficit in PACG [45]. Since PACG typically progresses silently and affects peripheral vision in its initial stages, perimetry is an essential tool for early detection, intervention and monitoring [51] [52].

2.5 Computerized analysis of eye images

Numerous research efforts have been dedicated to automating glaucoma detection using various types of ophthalmic imaging. This section explores these approaches, categorized according to the imaging modalities employed.

2.5.1 Van Herick

Only a few research groups have focused on using Van Herick images to classify PACG, with most relying on labeled datasets for training. One research group produced four articles on this topic [53] [54] [55] [56].

The first work used Van-Herick images to validate the positioning of the slit light on the eye. They trained a CNN (AlexNet) with Van Herick images labeled based on three different light placement: on the scleara (left), on the limbus (center) and on the iris (right). After applying data augmentation to balance the dataset, they obtained precision and recall values above 80% [53]. This algorithm's primary purpose was to select and validate the suitable image for future ACD measurement. Building on their work, their second study compared CNN architectures (AlexNet and VGG-16) and achieved precision and recall values surpassing 86% for the suggested architectures [54] using 8677 annotated images. Their following work [55] added 2 architectures, GoogLeNet and ResNet and compared all four to predict Van Herick grades (4 classes). Their overall accuracies for all four models were of 78.6%, 82.1% and 78.6% [55]. Lastly, they optimized their approach and achieved an agreement rate exceeding 66% across all four classes when compared with clinical grading. Additionally, grading errors were limited to a difference of only one grade [56]. One notable limitation of their work is the issue of generalizability. During image acquisition, they introduced a light pointer to guide the patient's gaze, resulting in white dots reflected at the center of the pupil. While these consistent markers likely assist in classifying the slit position, they may also compromise the approach's generalizability, as such conditions might not be easily replicated in other setups.

Simpler architectures were explored by [57]. They used a Support Vector Machine (SVM) algorithm for binary classification of Van Herick images into 2 categories: angle-closure likely or unlikely. The input parameters are the measured thickness of the AC and the cornea. Gonioscopic examination was performed on all participants and served as the baseline for evaluation. The model achieved an overall accuracy of 90%, with a sensitivity of 62.5% and a specificity 95.2% [57]. Some notable limitations of this work is the data dependency. The dataset only consists of 50 images, limiting the generalizability of the proposed method.

2.5.2 OCT images

Some studies use OCT images to evaluate the ACD and train a model to classify PACG patients paired with annotations from experts. [42] trained a multivariable logistic regression to predict PACG patients from swept-source OCT results. With a training dataset of 2928 images and a validation dataset of 1176 images, they obtained a 90.2% sensitivity and 85.2%

specificity [42]. [43] proposes a multi-sequence deep network to classify AC angles into 3 classes, open angle, appositional and synechial angle (the latter 2 are closed angles that differ in their mechanism). They used anterior segment OCT (AS-OCT) in bright and dark conditions and achieved an accuracy of 91% [43].

2.5.3 Multi-modal approach

Images of the anterior eye segment hold the potential for revealing signs of systemic diseases. [58] explores the diagnosis capabilities of deep learning models trained on these images to detect signs of conditions such as diabetic retinal disease, poor blood sugar control, elevated lipid levels and cataracts. This work serves as a foundation for further exploring the use of anterior eye segment images for diagnosis purposes.

Few previous works are using anterior segment images for PACG detection, coupled with annotations from other imaging modalities such as OCT. [59], [60] and [61] utilizes smartphone-acquired images from a slit-lamp, paired with a deep learning algorithm and OCT measurements of the anterior chamber depth (ACD). Using a modified residual network 34 for ACD predictions, [59] achieved a sensitivity of 85% and a specificity of 84%. It is important to note that this study was done on patients aged 11 to 15 years old with no PACG cases. [60] used a SWSL ResNet for the ACD estimation model and their sensitivity and specificity are 94.3% and 90.2% respectively for angle-closure risk prediction. [61] used 66 samples of participants of 60 y.o or older to train a random forest algorithm to estimate the ACD to obtain an out-of-bag prediction R^2 of 0.73 [61].

Other previous works use AS-OCT paired with gonioscopy examination. [62] developed a convolutional neural network classification model using AS-OCT images with gonioscopy gradings from ophalmologists as labels. Their algorithm was tested on 3 different databases, the Chinese American Eye Study, a clinic in Singapore and a hospital at the University of Southern California, they obtained an area under the curve (AUC) of 0.92, 0.89 and 0.92 respectively. [63] used the same database as [62] and developped 3 multiclass models for gonioscopy grading's classes, a ResNet-18, an Inception-v3 and a custom CNN. They obtained an AUC of 0.933, 0.901 and 0.910.

2.5.4 Fundus images

Other groups utilize fundus images (retina) and the cup to disc ratio (CDR) to detect glaucomatous damage (as explained in section 2.4.4). For instance, [64] developed a deep learning

algorithm that uses fundus images, achieving accuracies of 0.8429 and 0.7495 on two different datasets. The same research group developed an architecture in [65] that segments the optic disc and optic cup and computes the CDR for glaucoma diagnosis. They acheived AUCs of 0.8019 and 0.8397 across two datasets [65]. Others [66] [67] attempted similar approaches and obtained a Dice score of 0.94 [66] and an accuracy of 90.0% [67]. [68] proposes an atlas framework to evaluate the disc excavation caused by glaucoma. They achieved an specificity of 90 with expert segmentations. Many research groups are working on fundus images to detect signs of glaucoma, including computing the CDR which is an indicator of disc excavation associated with deterioration of the optic nerve [29].

CHAPTER 3 RATIONAL AND OBJECTIVES

Primary angle closure glaucoma (PACG) is a significant cause of vision loss globally, particularly in aging populations and among certain ethnic groups. Due to its rapid progression and the irreversible nature of the vision loss it causes, early detection is crucial. However, conventional diagnostic methods for PACG, such as gonioscopy, Optical Coherence Tomography (OCT), and tonometry, present challenges in terms of accessibility, cost, and patient comfort. These methods often require specialized equipment and trained professionals, limiting their availability in resource-constrained or remote settings.

This project aims to investigate the viability of a non-invasive, cost-effective approach to PACG detection using external eye images. By focusing on the Van Herick test, which assesses the anterior chamber angle using a slit lamp without direct eye contact or pupil dilation, this study seeks to simplify and automate the diagnostic process. Integrating this approach with image processing algorithms may allow for automated, efficient PACG screening, thereby expanding access to eye care, particularly for patients in rural or underserved areas.

Due to the limited number of images and lack of annotations (306 labeled images from the initial 2490), this study relies on classical image processing and segmentation techniques rather than machine learning. Without labeled datasets, it is unfeasible to train a deep learning model effectively. Instead, traditional image analysis methods are used to process and evaluate the visual information from the Van Herick test images, as explained in the literature review.

The primary objective of this research is to develop and evaluate an automated diagnostic algorithm for detecting signs of PACG using external eye images, specifically focusing on images obtained through the Van Herick test. This study also aims to support the broader goals of teleophthalmology by contributing to the development of remote, accessible diagnostic tools that can aid in the early detection and management of glaucoma.

The primary objective can be divided into **three specific objectives**:

- **Dataset construction:** The initial dataset was provided by LightX from the Laurentides Eye Institute. However, most images are from patients with PACG, both pre- and post-operative, resulting in an unbalanced distribution across PACG grading levels. To address this, we collaborated with LightX to conduct additional data collection at Polytechnique, mainly targeting students in particular, as PACG prevalence is low in young individuals.

- **Automated anterior chamber angle ratio calculation:** Develop an automated method to calculate the anterior chamber angle ratio, a key indicator for assessing PACG risk. This calculation involves segmenting the anterior chamber and corneal thickness, then estimating the ratio of anterior chamber depth to corneal thickness based on Van Herick test images. An intermediate step in the ratio calculation is the segmentation of the light slit projected onto the cornea and its reflection. Classical image processing techniques are used for this step, enabling the results to be used for automatic labeling of images. This labeling process will support future research and facilitate machine learning applications by generating labeled data for model training in subsequent studies.

- **Evaluation using clinical annotation done by an ophthalmologist:** Validate the effectiveness of the automated ratio calculation and the diagnostic algorithm by comparing it to clinical annotations provided by an ophthalmologist. These annotations, which include angle grading for part of the dataset, will serve as a benchmark, allowing for a comparative assessment of the algorithm's accuracy in identifying PACG risk levels in a subset of the dataset (12%) for which annotations are available. The lack of comprehensive annotations across the entire dataset presents a challenge but also highlights the importance of developing reliable automated methods to assist in clinical evaluation where annotations are limited.

CHAPTER 4 METHODOLOGY

The main goal of this project is to detect and classify the risk of primary angle closure glaucoma (PACG) using external eye images, specifically through the analysis of Van Herick test data. To achieve this, an automated pipeline has been developed, using several techniques in image processing. This section details the methodology employed, including data collection, preprocessing, region of interest (ROI) selection, slit extraction, ratio calculation as explained in section 2.4.1 (figure 2.5) and validation.

4.1 Database

The dataset was provided by our partners for use in the project, and was collected at the Institut de l'Oeil des Laurentides (IOL), comprises a total of 14990 images, with some being stereoscopic images, including 2490 Van Herick images.

However, several issues were identified with the provided databases. A notable proportion of the images are post-operative, particularly in patients previously diagnosed with PACG who have undergone laser peripheral iridotomy (LPI). The visibility of the drainage hole in these images is a limitation as it affects the shape of the light beam reflection on the iris and reduces their diagnostic value. In addition, many images are invalid, for example, some images were mislabeled as Van Herick when they were of a different test type or a miss-click (figure 4.1 (c)), while others suffer from issues such as overall blurriness or focusing on the incorrect ocular structure (figure 4.1 (a)). These problems contribute to increased variability within the dataset, posing challenges for the development of a robust and generalizable algorithm. Therefore, the acquisition of a normative database is a necessary step to address the limitations of the IOL dataset.

4.1.1 Data collection protocol

We obtained ethical approval from Polytechnique Montréal's Ethics Committee (CER-2223-75-D) (Appendix C) to recruit a total of one hundred participants, from Polytechnique's community, for acquiring images of the anterior segment of the eye. Collaborating with Dr. Sébastien Gagné, an ophthalmologist and a member of our industrial partner LightX, we conducted image acquisition for seven tests: conjunctiva, cornea, anterior chamber, pupillary margin, Van Herick, lens, and iris trans-illumination (Figure 4.2). The resulting dataset will be referred to as Poly dataset.

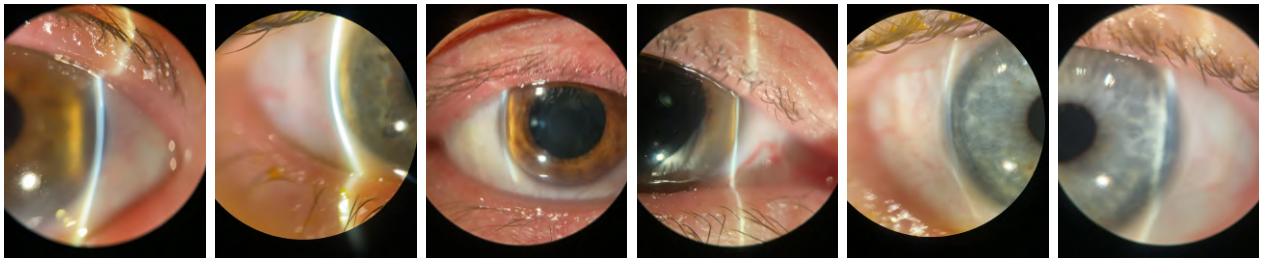

(a) Blurry images

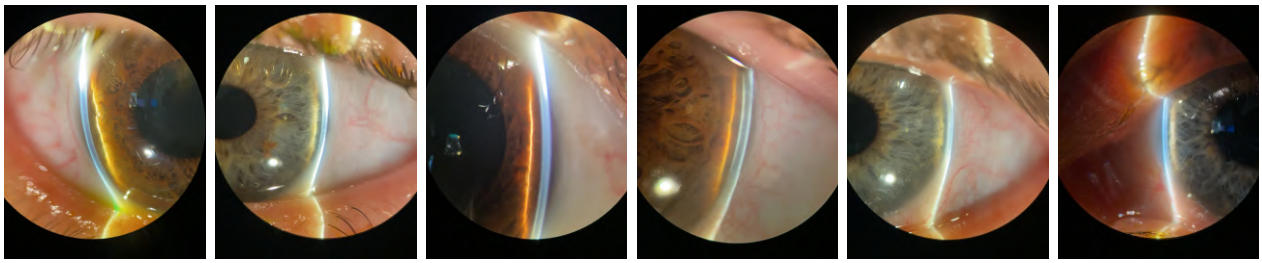

(b) Valid images

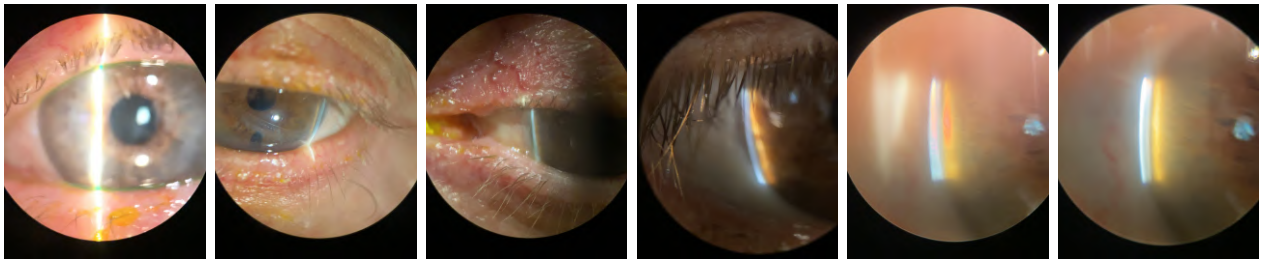

(c) Invalid image acquisition

Figure 4.1 Sample Van Herick images from the IOL database

Participants of all genders, ages, and ethnic origins were included, while individuals with a history of glaucoma, diabetic retinopathy, macular degeneration, cataracts, or vision loss were excluded.

In addition to anterior eye segment images, demographic data such as age, gender, ethnic origin, and known optical correction were collected.

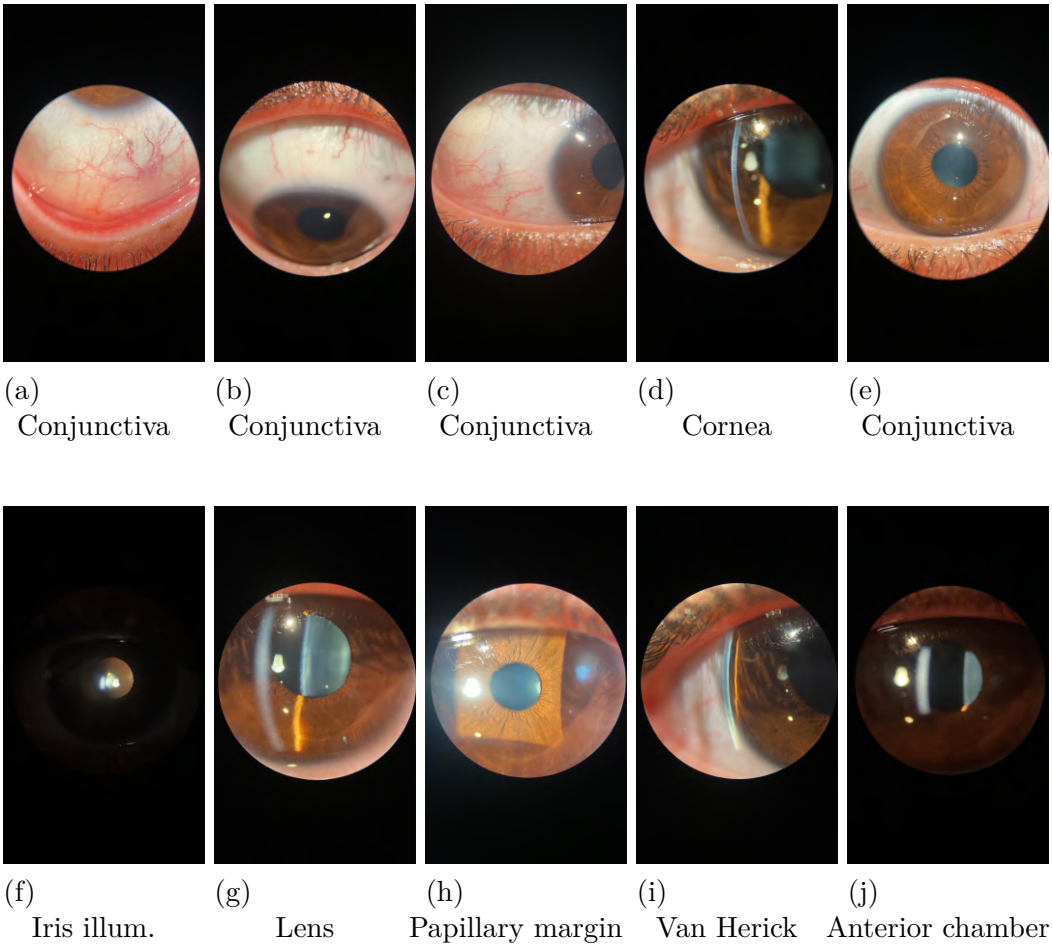

Figure 4.2 Sample test images.

4.1.2 Image annotation

Each dataset includes annotations provided by an expert ophthalmologist specialized in glaucoma, indicating the clinical grading of the anterior chamber angle in terms of Van Herick ratio. Images from Poly dataset were all non-pathological and were labeled with a ratio of 4/4. For the images from the IOL database, 306 out of 2490 images were annotated with one of the following labels: 1/4, 1/4 - 2/4 (both ratios are valid), 2/4, 3/4, and 4/4.

4.1.3 Dataset Overview

The dataset used in this research consists of eye images collected from two different sources, ensuring diversity in patient demographics, imaging conditions, and ocular characteristics. It comprises all the annotated images from the IOL dataset, which primarily contains post-

operative images from glaucoma patients, and all images from Poly dataset, comprising non-pathological images. The RGB image sizes are 3413 x 1920 pixels for the Poly dataset and 4224 x 2376 pixels for the IOL dataset.

4.2 Color analysis

Van Herick images are color images encoded on the three red, green and blue channels. The first processing step was to explore different color models to determine the optimal color channel or combination of channels that minimizes noise and maximizes the contrast of the light slit for easier segmentation. RGB, HSV, Luv, CIE-Luv (standard color space defined by the International Commission on Illumination (CIE) [69]) , YUV and YIQ (Y: luminance, U, V, I, Q: color information) [70] color models were considered, and a qualitative comparison of the different channel decomposition on a same Van Herick image is provided in 4.3.

The RGB and Luv color channel decomposition were selected for the following steps in the pipeline. The light slit color across different images was more consistent while using these channels than with the rest, which is important to limit the variability in images.

4.3 Automatic selection of the ROI

Due to variability in images across the dataset and inconsistencies in texture and color within each image, directly segmenting the light beam across the entire image presents significant challenges and is highly sensitive to noise. The manual mounting setup of the slit lamp causes variability in the position and size of the circular mask created by the binoculars' shape. Additionally, eye color impacts the intensity, sharpness, and colors of the projected light slit on the cornea and its reflection on the iris (Figure 4.1).

For darker irises, the main slit appears blue, and its reflection is yellow, providing relatively good contrast for segmentation. Conversely, for blue irises, the slit lamp operator must decrease the light intensity, which reduces the sharpness of the slit's contour . The reflection on blue irises appears beige/yellow, causing the contours to be blurred and blend with the visible texture of the eye. Consequently, the color contrast between the slit and the iris is significantly lower for blue eyes compared to darker eyes, which affects texture and decreases contour sharpness.

To address these challenges, a preliminary step involves approximating the position of the vertical slits before proceeding with the segmentation.

Prior to the slit segmentation, two ROI masks were implemented. The first was a circular

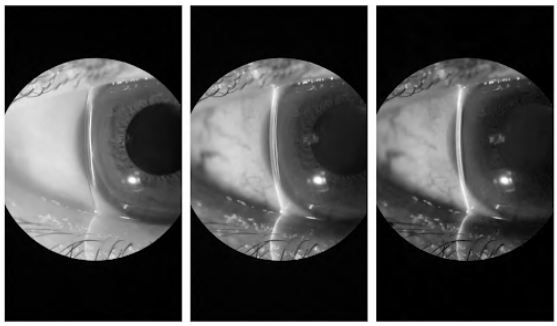

(a) Red, green, and blue channels

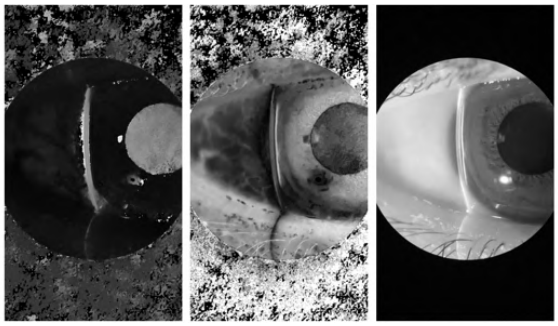

(b) Hue, saturation, and value (HSV)

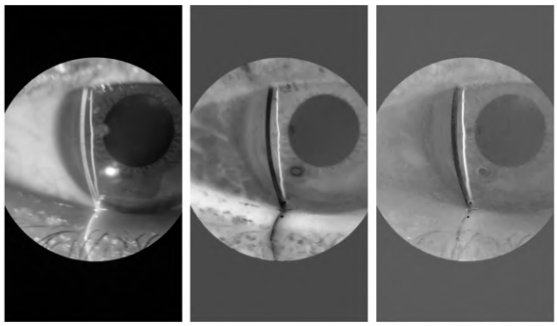

(c) Luv [69]

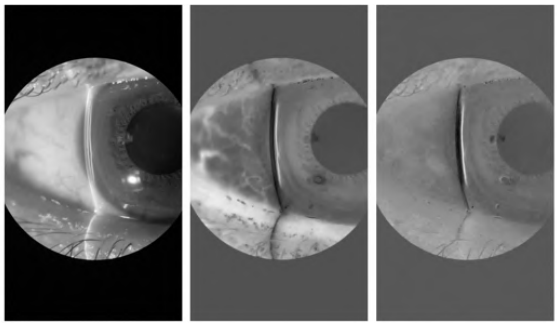

(d) cie-luv [69]

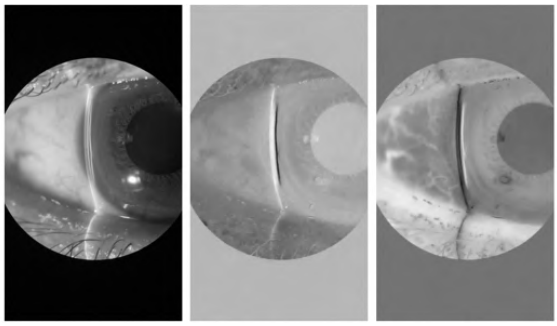

(e) YUV [70]

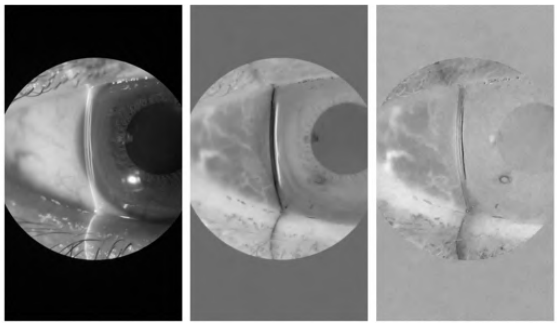

(f) [69]

Figure 4.3 Channel Decomposition

mask corresponding to the visual field of the bio-microscope binoculars (see section 4.3.1),and the second was a rectangular mask around the light slits (section 4.3.2).

4.3.1 Circular ROI mask

The first step involved applying simple thresholding using the triangular method. The contours of the resulting binary mask were then extracted using the `cv.findContours` function from the OpenCV library. These contours were used to fit a parametric circle with the

`cv.HoughCircles` function. This three-step approach facilitates precise identification of the circular shape of the binoculars in the images. It ensures a circular output, as opposed to using thresholding or contour detection alone, which results in oddly shaped masks, or directly applying the Hough transform algorithm (Appendix A). The latter is highly sensitive to image texture and can detect multiple circles if used directly on the image.

4.3.2 Rectangular ROI mask

The light slit projection onto the spherical shaped anterior segment of the eye, exhibits a slightly curved shape, resembling arc segments of large circles, larger than the image itself. While the Hough Transform for circle detection is theoretically a viable option, its effectiveness is limited due to the significant difference in size between the circles formed by the slit arcs and the overall image. This technique transforms the image into a parameter space and uses an accumulator to count votes for all possible circle coordinates at each pixel. However, in our case, the center coordinates of the arcs lie outside the image boundaries and must also be represented in the parameter space. This significantly increases the parameter space dimensions, resulting in higher computational costs and extended processing time.

Inconclusive experiments

Several methods were explored and subsequently abandoned due to their limitations or inconclusive results. Before deciding to limit the image size by selecting a rectangular ROI, slit detection was attempted on the entire image using various approaches, including:

- Multi-class thresholding,
- K-means clustering with varying k-values,
- Canny edge detection with varying k, t_{high} and t_{low} values
- A gradient middle line applied to the edge filter output,
- A modified gradient line approach using a window of variable heights to minimize noise effects.

These methods were ultimately deemed unsuitable due to high sensitivity to noise. Detailed descriptions of these experiments are not included in this document.

Chosen method

A more efficient approach was to use the Hough Transform to detect vertical lines. By analyzing the horizontal gradient and applying a threshold to the angles of detected lines, this method can filter out irrelevant lines. Ensuring fast and reliable detection of light slits by evaluating the line length and point gaps. The chosen method consists of the following steps:

1. Decreasing by 5% the radius of the circular ROI mask, to avoid detection of the contour and ensure the absence of background in the segmented image.

2. Applying a horizontal gradient using a Sobel high pass filter with a standard kernel size of 3x3, including a Gaussian filter to smooth the image.

3. Using `cv.HoughLinesP` on the resulting gradient image. The OpenCV library provides two implementations of the Hough Transform for line detection: the standard and the probabilistic methods. The probabilistic method, being more efficient [71], was chosen for this step as it allows fine-tuning of parameters such as `minLineLength`, `maxLineGap` and `threshold` on the cumulative vote. Additionally, a range threshold was applied to the angle of the detected lines relative to a vertical orientation, as the light slit is consistently vertical. A qualitative, manual comparison was conducted to evaluate the effects of varying angle ranges, minimum line lengths, and maximum gaps between points considered part of the same line on a subset of images. The optimal parameters that successfully detected the slit while minimizing peripheral noise were determined to be: an angle threshold of $\pm 30°$, a minimum line length of 300 pixels, and a maximum gap of 10 pixels.

   In the event that no lines are identified with the specified parameters, their values are automatically adjusted. Specifically, the minimum line length requirement is decreased by 20 pixels, and the maximum gap is increased by 2 pixels at each iteration until a vertical line corresponding to the approximate position of the slit is detected. In instances where the image quality is insufficient for line detection, the algorithm selects a random region of interest (ROI) window at the center of the image, which is presumed to be the most probable position for the slits. It is noteworthy that the orientation angle range is not adjusted, as the biomicroscope light beam is consistently oriented vertically.

   The final rectangular segmentation of the region of interest is presented in figure 5.5.

4.4 Slit segmentation

After narrowing down the image area, the next step was to perform a color channel analysis to determine the best image representation that enhances the object of interest. Following the conclusions of the initial color analysis (section 4.2), the three channels of both RGB and LUV decompositions were used again for the subsequent experiments presented in figure 4.4. The chosen approach was to select the longest line using the results on all 6 channels, limiting errors due to noise.

1. Preprocessing:
    - Apply 25 x 25 Gaussian mask to smooth the input image and attenuate the noise.
    - Compute the horizontal gradient of the blurred image to highlight edges using a Sobel filter of size 3 x 3.
    - Normalize the horizontal gradientfor better visualization using the `NORM_MINMAX` method [72].
    - Apply an adaptative binary thresholding on the normalized contour image by computing the intensities along every row and only keeping the 20 highest values. Using a fixed thresholding is not suitable in this step due to the high variability in our images.
    - Generate binary masks for red, green, and blue channels, based on the max intensities of each image (adaptative binary thresholding).
    - Combine the three masks into one single channel image using `np.logical_or`. As shown in figure 4.4. None of the individual R, G and B channels distinguish both slits perfectly, neither do the L, U, V channels. However, combining the R, G and B masks resulting from the edge detection, normalization and thresholding enhances all the structures of interest.
    - Skeletonize the RGB-combined mask to represent the main structure of the detected features with one-pixel width lines.
    - Refine the skeleton using contour analysis to eliminate small noise components by applying the `cv.findContours` function from the OpenCV library, this step removes noise caused by the eyelid and lashes. Followed by another skeletonization to obtain clean lines Figure 4.5.
2. Slit Segmentation

- Implement a connected component analysis (CCA) on the resulting image, only keeping the longest 4 elements.
- Depending on the image quality, the result of the CCA could present some issues, such as disconnected components: where the same curve is split in two. An optimization to correct this is to find all endpoints and compare them in pairs, the starting point of element 1 and the end point of element 2. If a set of conditions is met, we connect the lines and consider them as one component. The chosen conditions are: the distance between the points, and the maximum angle difference between the tangential lines at both endpoints. Different values were manually tested and qualitatively evaluated and the resulting criteria are a maximum distance of 50 pixels and a maximum angle difference of 10 degrees. Increasing one or both values tends to connect 2 curves that are corresponding to different slits.
- The result consists of 4 distinct binary masks, representing the 4 slit contours, three examples are provided in figure 5.8.

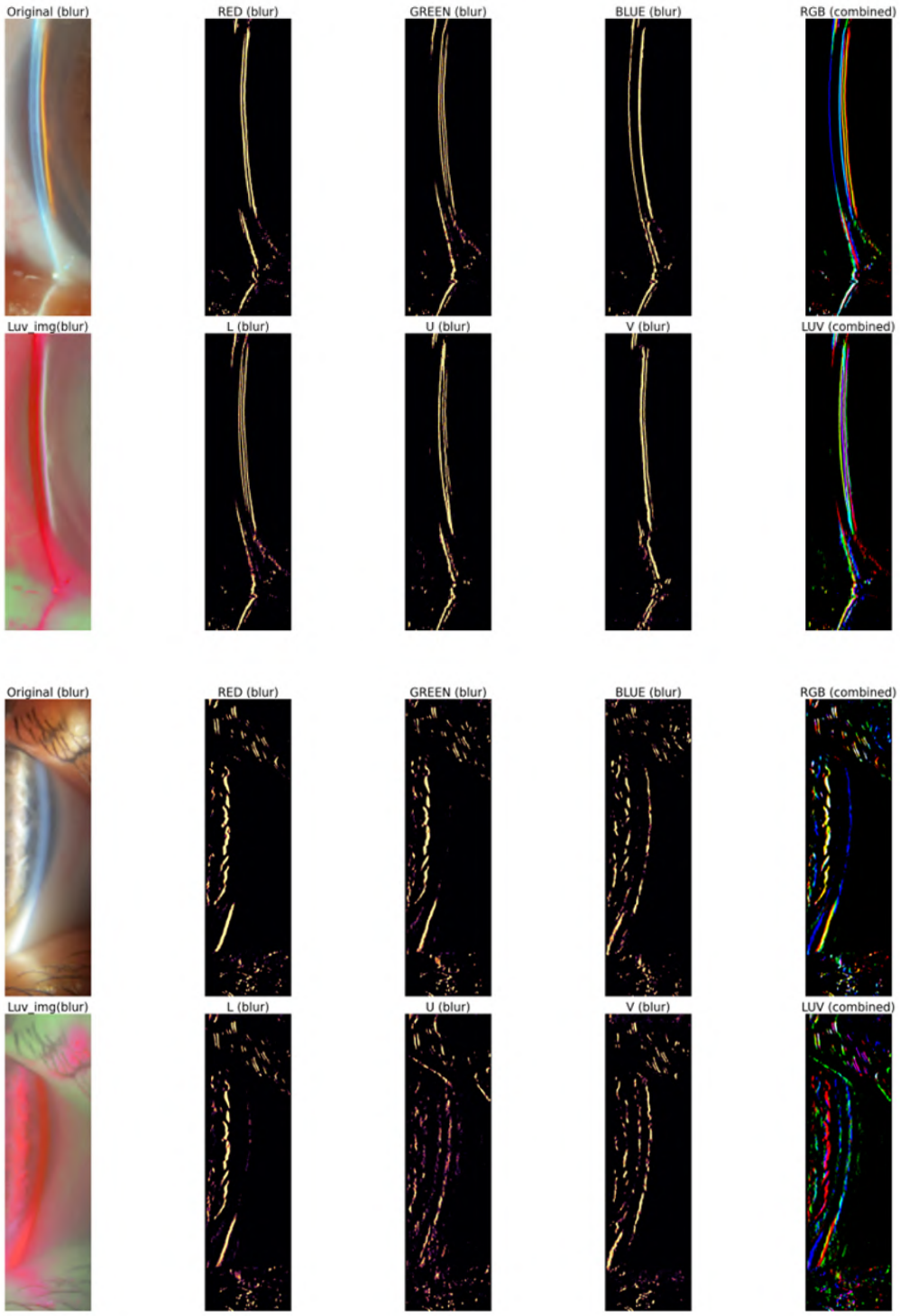

Figure 4.4 Color channel decomposition for the ROI

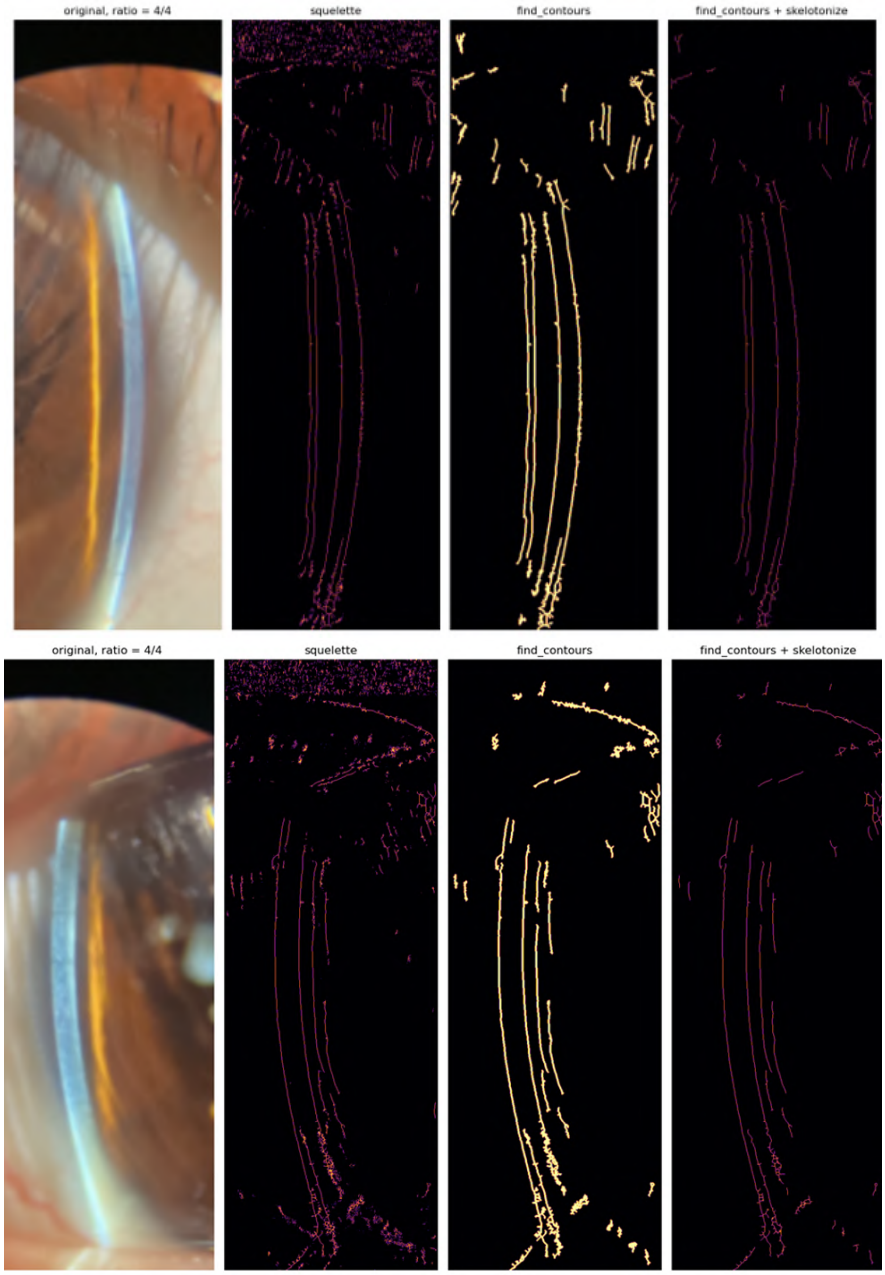

Figure 4.5 Skeleton refinement

4.5 Parametric curve fitting

to guide the circular parametrization of the arcs, a pupil position detector was implemented by computing the center of mass of the histogram of the left and right halves of the image. Following pupil localization, the `fit_arc_circle` function is implemented and applied to the masks of the longest detected curves. This process involves fitting arcs that approximate the

shape of the slits, capturing their curvature and orientation. The previously identified pupil position plays a crucial role by aligning the results with the anatomical expectations of the analysis. This alignment minimizes errors and provides a robust foundation for subsequent measurements and classifications.

Multiple methods were explored during the development process, notably the use of the gradient change along a horizontal line and a horizontal window. These methods were not generalizable, were very sensitive to noise and produced highly variable results. Appendix B illustrates the results of the inconclusive gradient method. The detailed steps of the final procedure are presented as follows for every individual slit mask:

1. The algorithm computes an initial estimate of the circle center (mean of x and y coordinates) and radius (mean distance from the center to all points on the curve). This serves as a starting point for circle fitting.

2. Using a least-squares optimization method, the initial guess is adjusted to minimize the algebraic distance between the curve points from the binary mask and the fitted circle. The algebraic distance function is a core component in circle fitting algorithms. This function calculates the deviation of points from a hypothesized circle, enabling optimization techniques like least squares to iteratively adjust the circle parameters for a best fit.

   The algebraic distance is expressed mathematically as:

   $$D = \sqrt{(x - x_c)^2 + (y - y_c)^2} - R \tag{4.1}$$

   where x_c and y_c are the coordinates of the circle center, R is the radius, and (x, y) represents a point on the curve.

   Given a set of points (x, y), the function computes the Euclidean distance from each point to the hypothesized circle center (x_c, y_c). This distance is then compared to the hypothesized radius R, and the difference is returned.

   The returned value represents the residuals for each point. By iteratively refining the parameters x_c, y_c, and R, the fitting process converges to a circle that best represents the input points.

3. The fitting process iterates until the circle center meets the expected position (left or right) or the maximum number of attempts is reached. If the expected position is not achieved, the function modifies the initial guess by flipping the sign of the x-coordinate to encourage fitting in the desired direction. If the maximum number of attempts

is reached without finding a suitable fit, a warning is logged, and the best-fit circle parameters up to that point are used.

4. After the circle coordinates are calculated, the algorithm computes partial arcs by determining the angles corresponding to the topmost and bottommost points of the curve of each binary mask. These angles are adjusted for image space and used to generate an arc between the start and end angles. The reason behind only displaying partial arcs is that the endpoints are used to find the best horizontal line along which to compute the distances between the lines for Van Herick ratio calculations. Extending a curve poses the risk of computing the distances at a point that does not represent the actual visible light slit.

5. Finally, the algorithm returns x and y coordinates of the fitted arcs, which will be used in the ratio calculations to generate Van Herick grading.

This function is highly adaptable and provides precise fits for light slits or other curve-like structures in segmented images. Its iterative fitting and fallback mechanism ensure relative robustness, even when initial guesses are less accurate.

4.6 Van Herick ratio calculations

The calculation of the Van Herick ratio involves identifying the optimal horizontal line, which is perpendicular to the detected curves, and measuring the distances between these curves along this line. This process is crucial for determining the anterior chamber depth and requires robust computational steps to handle variability in the curve positions and shapes.

4.6.1 Finding the Optimal Perpendicular Line

The implemented function `find_optimal_perpendicular_line` identifies the horizontal line that best approximates perpendicularity to the tangents of the detected curves. This ensures accurate measurements for subsequent ratio calculations. The procedure involves:

1. Curve Filtering: This step ensures that only valid curves are considered for further analysis by filtering out outliers. The function evaluates the vertical extents (minimum and maximum y-coordinates) of all detected curves. A curve is deemed valid if its vertical range overlaps significantly with other curves' ranges. For instance, the topmost point of one curve must lie below or at the bottommost point of another, ensuring a continuous overlap across valid curves. By isolating curves with shared regions of

interest, this filtering step focuses the analysis on meaningful structures while excluding noise or irrelevant segments. To compute the ratio for the Van Herick grading, only 3 curves are needed: the inner and outer edge of the projected slit and the outer edge of its reflection. The distance between the first two curves represents the thickness of the projected slit, and the distance between the second and third one represents the space between the projected slit and its reflection (figure 2.5). Consequently, if there are less than 3 valid curves, it is impossible to compute the ratio, and the image is skipped.

2. Tangent Calculation: In general, the curves corresponding to the projected slit contours are often better detected than the reflection. This function identifies the two most prominent curves in the image that correspond to the projected slit contours. The tangents to these curves are calculated at various points to approximate their local slopes. These tangents are used as a reference to determine a horizontal line that is as perpendicular as possible to the slopes of the curves, providing a reliable basis for further measurements, such as the Van Herick ratio.

3. Iterative Line Evaluation: The function then iterates over all potential horizontal lines within the bounds of the detected curves, comparing their alignment with the calculated tangents. The line that achieves the best perpendicularity is selected.

4. Fallback Mechanism: If no suitable perpendicular line is found, the function defaults to the horizontal line passing through the middle of the image. This fallback often coincides with the convex maximum of the curves if the rectangular ROI is appropriately determined.

4.6.2 Van Herick Ratio Classification

Once the optimal perpendicular line is identified, the `classify_van_herick` function calculates the distances between the detected curves along this line. These distances are used to compute the Van Herick ratio, a metric for assessing anterior chamber depth. The process involves:

- Intersection Identification: For each valid curve, the intersection point with the optimal line is determined.

- Distance Measurement: Distances between consecutive intersection points are calculated, providing the values $d_{1,2}$ and $d_{2,3}$. The pupil position parameter is used again to determine the direction of computing. If the pupil is on the right, we start from the left, and vice versa.

- Ratio Calculation: The numerical ratio Van Herick Ratio = $\frac{d_{2,3}}{d_{1,2}}$ is computed.
- Grading classification: Based on predefined thresholds, the ratio is classified into categories (1/4, 2/4, 3/4 and 4/4) for clinical interpretation. Identify the closest classification threshold c_{closest}:

$$c_{\text{closest}} = \text{argmin}_{c \in C} |c - R| \tag{4.2}$$

where R is the computed Van Herick ratio and C is the set of predefined classification thresholds. Ambiguities between categories are resolved by considering the error margin of 0.05 and proximity to thresholds, if the difference between 2 ratio classes is less than the error margin, then the ratio is ambiguous, and both classifications are reported with their respective probabilities. Otherwise, the ratio is assigned to the closest classification.

4.7 Evaluation

The evaluation of the segmentation and classification pipeline involved a set of experiments using both the IOL and Poly datasets. The performance of the pipeline was assessed using qualitative and quantitative methods.

The automatic selection of the circular and rectangular ROIs, slit segmentation, and parametric curve fitting were qualitatively evaluated and iteratively optimized during the project. For the ratio calculations and Van Herick classifications, annotations provided by an expert ophthalmologist enabled quantitative validation. Standard metrics—precision, recall, accuracy, and F1-score—were applied to quantitatively measure the algorithm's effectiveness, particularly its ability to correctly identify high-risk PACG cases.

$$\text{Accuracy} = \frac{\text{TP} + \text{TN}}{\text{TP} + \text{FP} + \text{FN} + \text{TN}} \times 100 \tag{4.3}$$

$$\text{Precision} = \frac{\text{TP}}{\text{TP} + \text{FP}} \times 100 \tag{4.4}$$

$$\text{Recall} = \frac{\text{TP}}{\text{TP} + \text{FN}} \times 100 \tag{4.5}$$

$$\text{F1 Score} = 2 \times \frac{\text{Precision} \times \text{Recall}}{\text{Precision} + \text{Recall}} \times 100 \tag{4.6}$$

The ratio calculation was evaluated on the Poly database, where all the data is non patho-

logical (1080 images classified as 4/4), on the subset of IOL database for which we have annotations (306 images), and for both subsets together (1386 total images with ratio annotations).

CHAPTER 5 RESULTS AND DISCUSSION

This chapter presents and discusses the results of the data collection, as well as qualitative intermediate results for some elements of the proposed pipeline, the quantitative results on IOL and Poly datasets and finally, qualitative results showcasing some satisfying results and highlighting encountered challenges.

5.1 Data Collection

In total, we collected 5,567 images in the Poly dataset, including 1,088 Van Herick images.

Regarding demographic distribution, Figure 5.1 highlights the diversity of the dataset in ethnic backgrounds. The median age of participants was 25 y.o., reflecting the recruitment of mostly students from Polytechnique Montréal during the data acquisition process. This younger demographic provides a complementary balance to the IOL database, which primarily consists of images from post-operative closed-angle glaucoma patients—an older population typically affected by this condition.

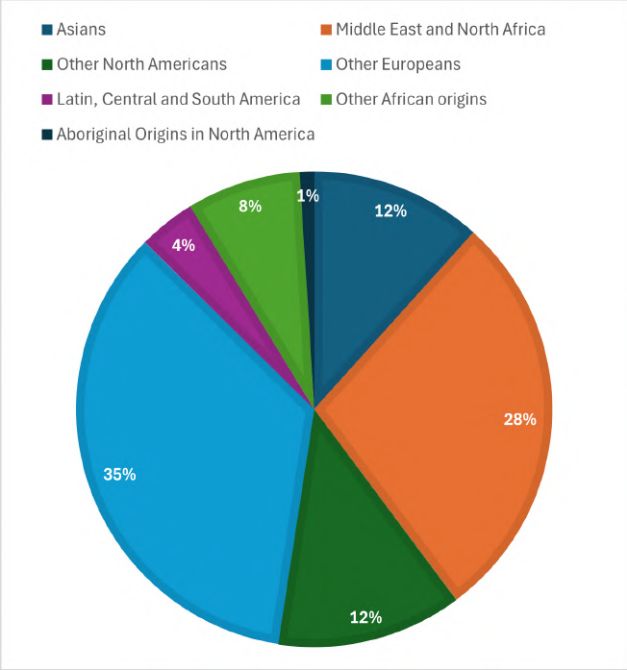

Figure 5.1 Demographic Distribution by Ethnic Origin in Polytechnique's Database

5.2 Automatic selection of the ROI

5.2.1 circular ROI mask

(a) Original image (b) Binary threshold (c) Contour detection (d) Final circle superimposed

Figure 5.2 Circular ROI detection as explained in section 4.3.1

Figure 5.2 illustrates one qualitative result of circular ROI segmentation. This process involves applying binary thresholding to the grayscale version of the original image, followed by contour detection and circle detection using the Hough Transform. As detailed in the methodology section, the radius of the detected circle is decreased by a factor of 5% to effectively eliminate background noise. Importantly, the object of interest (the slit) is consistently closer to the center of the circle than its edges, ensuring that this reduction in the circle radius has no negative impact on the subsequent processing.

5.2.2 Rectangular ROI mask

Building upon the circular mask, reducing the mask radius has shown improved results for rectangular ROI detection (Figure 5.3). This adjustment ensures that no background or contour pixels are included in the final image, enhancing the precision of the segmentation process. Figure 5.4 illustrates the intermediate results of the ROI detection algorithm, as detailed in Section 4.3.2.

The evaluation of this task is qualitative. Figure 5.5 provides a sample of cropped images showcasing the slit position approximation. For the vast majority of images in both datasets, the rectangular ROI window effectively surrounds the slits. This robustness can be attributed to two specific design choices:

- Line Detection Across Multiple Channels: By applying the Hough Transform line detector to the R, G, B, L, U, V, and gradient images (figure 4.5), the method avoids relying on any single step. Instead, it uses the longest detected line across multiple channels, ensuring reliability.
- Fallback Mechanism: If none of the six line detection attempts produces a line that meets the length and orientation criteria, a centered ROI window is selected as a fallback. This strategy increases the likelihood of approximating the slit position, even in challenging cases.

These choices ensure the algorithm's robustness and adaptability across diverse image conditions.

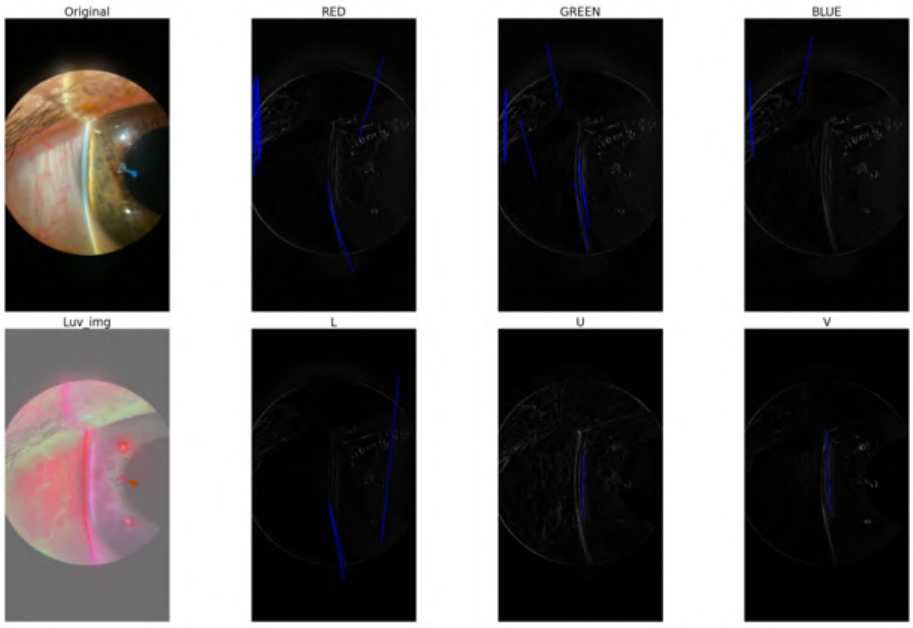

(a) Hough Lines algorithm for ROI approximation with the original circular mask

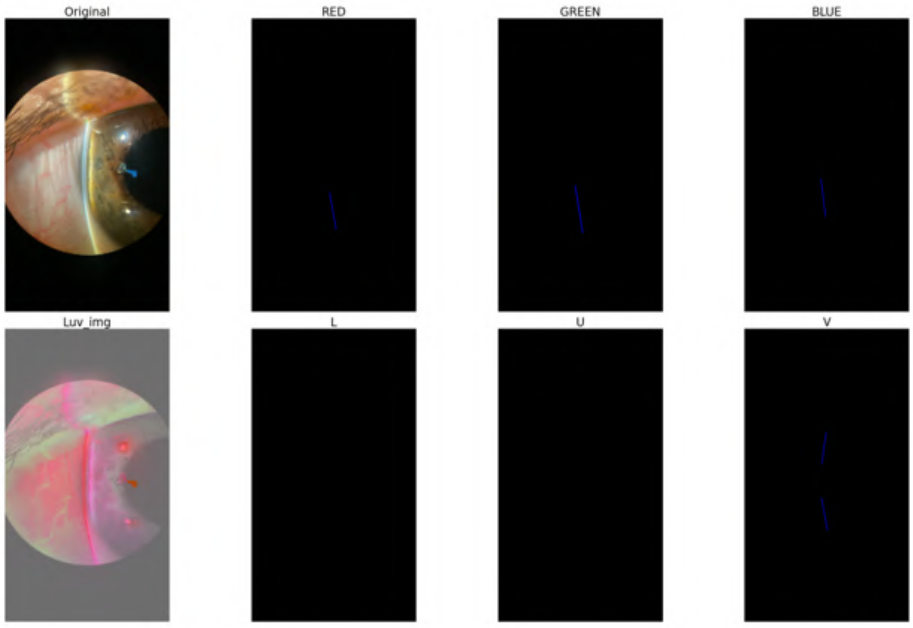

(b) Hough Lines algorithm for ROI approximation with the zoomed circular mask (0.9X)

Figure 5.3 Effect of reducing the size of the circular mask on the rectangular ROI approximation

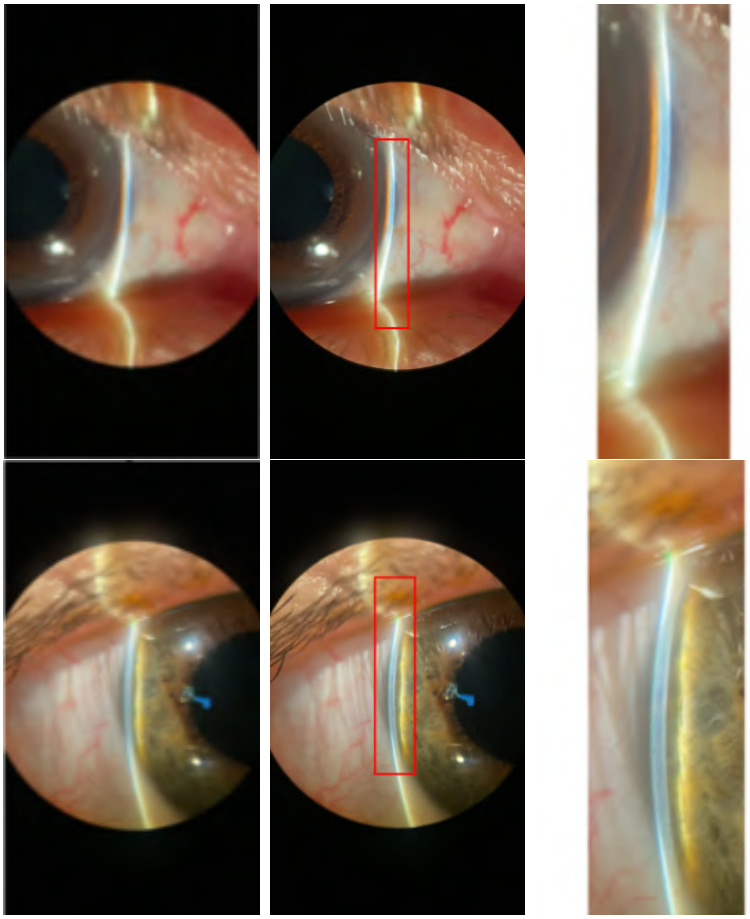

Figure 5.4 Results for the rectangular ROI detection algorithm. From left to right: original image, sobel horizontal gradient output, hough line detection, ROI on the gradient image, the original image and ROI cropping.

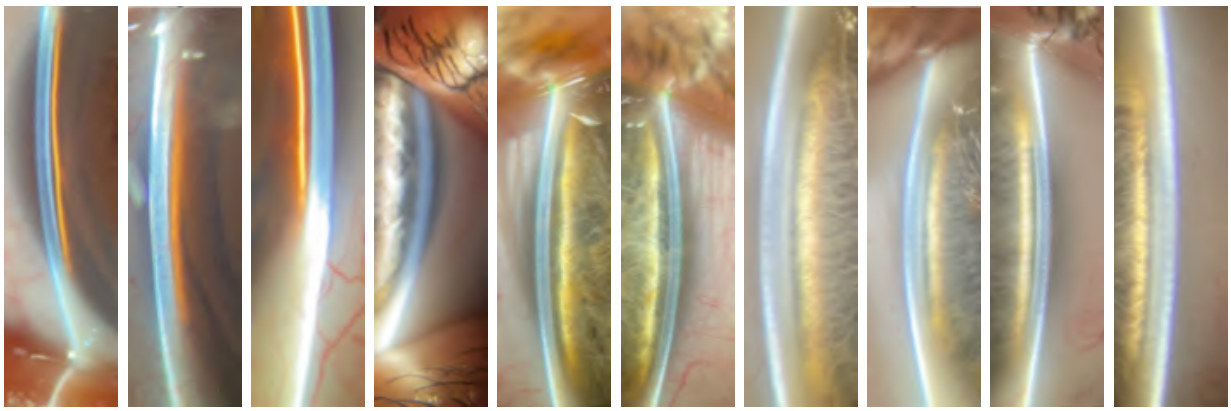

Figure 5.5 Results for the rectangular ROI detection algorithm on a subsample of data

5.3 Slit segmentation

In this step, the horizontal gradient of the cropped image was computed and thresholded for binarization. The skeletonization function was then applied to reduce the detected curves to one-pixel thin lines. As shown in Figure 5.6, noise is visible around the pupil and lashes. To address this issue, the contours of the skeleton elements were computed (third image), followed by another skeletonization step. The last two images in the figure illustrate the results of the connected component analysis (CCA) applied to the refined skeleton. The difference in the final image is that the contours were recomputed for better visualization and qualitative evaluation.

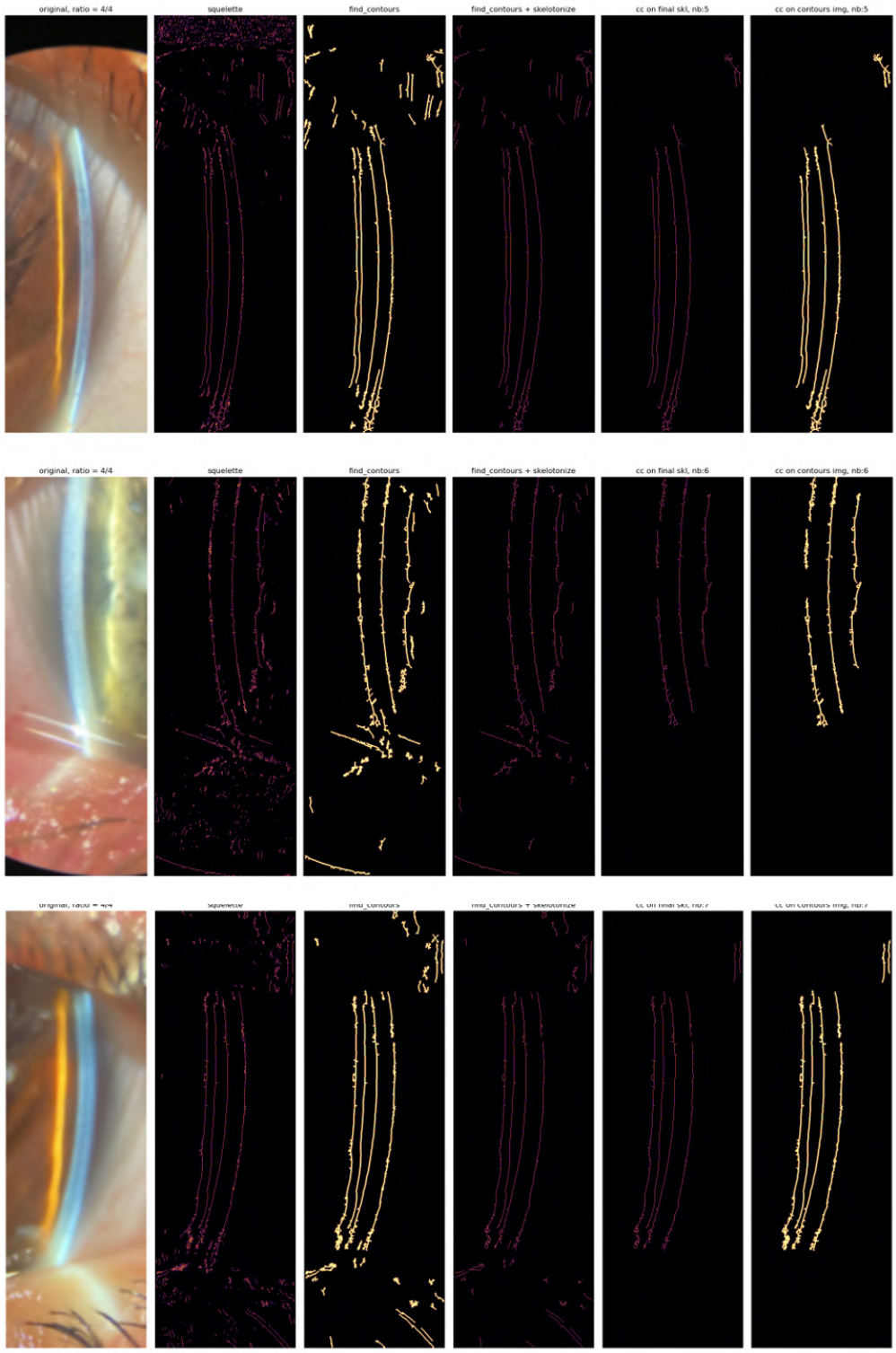

Figure 5.6 Sample skeleton refinement results on horizontal gradient of the cropped ROI image and Connected Component Analysis, displaying the longest elements, for three images.

Despite the improvements, this method has limitations. Some lines remain disconnected, leading to multiple curve detections for the same structure. This results in invalid ratio calculations. To resolve this, an algorithm was implemented to connect curve endpoints based on distance and orientation criteria, as detailed in Section 4.4. The results are shown in Figure 5.7. The algorithm successfully connects disconnected components if they are sufficiently close and their endpoints' tangents align in similar directions. However, the method does not connect all lines, as the criteria are intentionally restrictive to prevent connecting unrelated structures.

Furthermore, many disconnected pairs involve one long curve and a much shorter curve. The shorter curve is typically filtered out during the CCA length-based filtering step and is not used in subsequent processes. While this means the connection is not fully restored, the shorter curve only minimally affects the curve fitting process by contributing additional points to the three main slit contours. An example of this is shown in figure 5.8(b) where the external curve is divided into 3, the shortest two components are discarded, connecting them would not affected the final elements' choice in this step.

Finally, after reconnecting incomplete curves, the 4 longest curves are extracted and 4 binary masks are generated, three example results are provided in Figure 5.8.

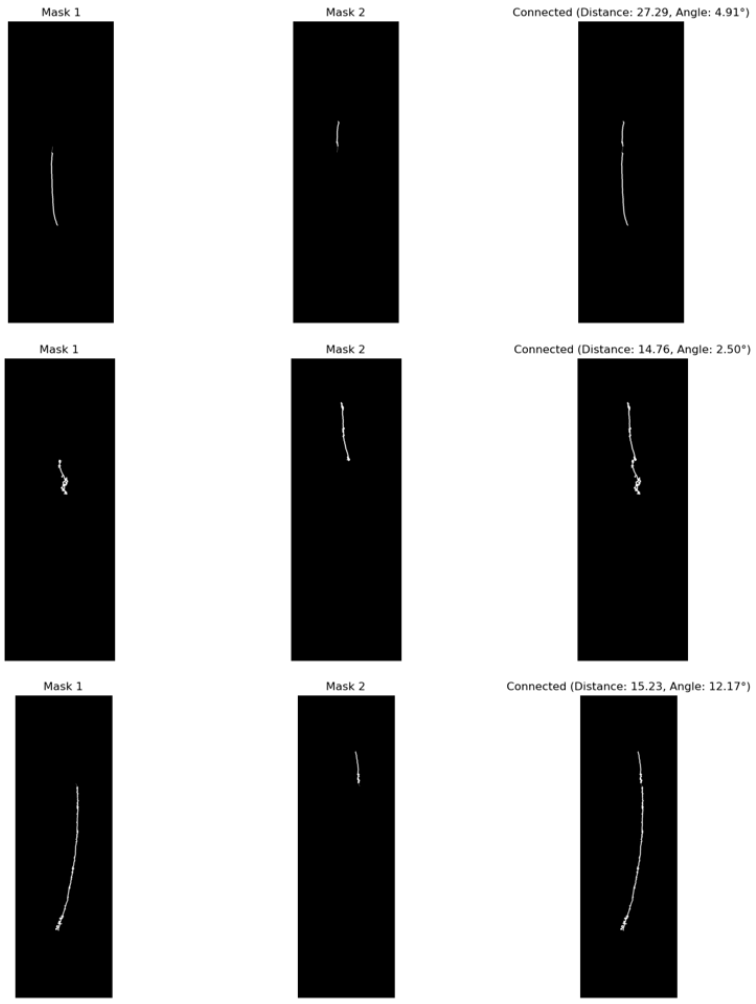

Figure 5.7 Result of the endpoint connection algorithm.

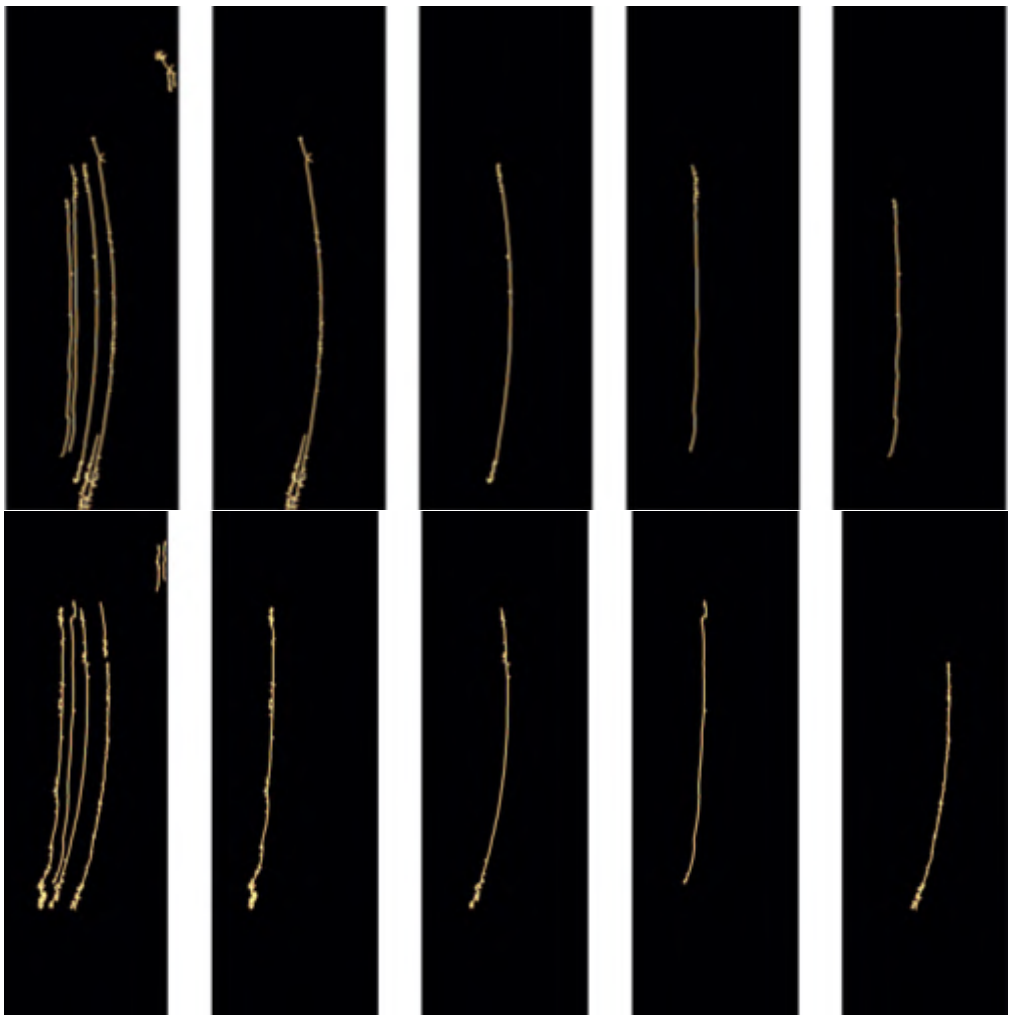

Figure 5.8 Selected connected components for parametric curve fitting

5.4 Parametric curve fitting

The first step is to find the position of the eye, which will determine the sign of the center's x coordinate as explained in the methodology section. Sample results of this step are presented in figure 5.9. This task was evaluated qualitatively for lack of annotations by iterating over many sample images. Because of the simplicity of this task, the qualitative evaluation was deemed enough to ensure its performance. THe arc circle fitting algorithm was them applied on the conected component masks. Results are shown in Figure 5.10

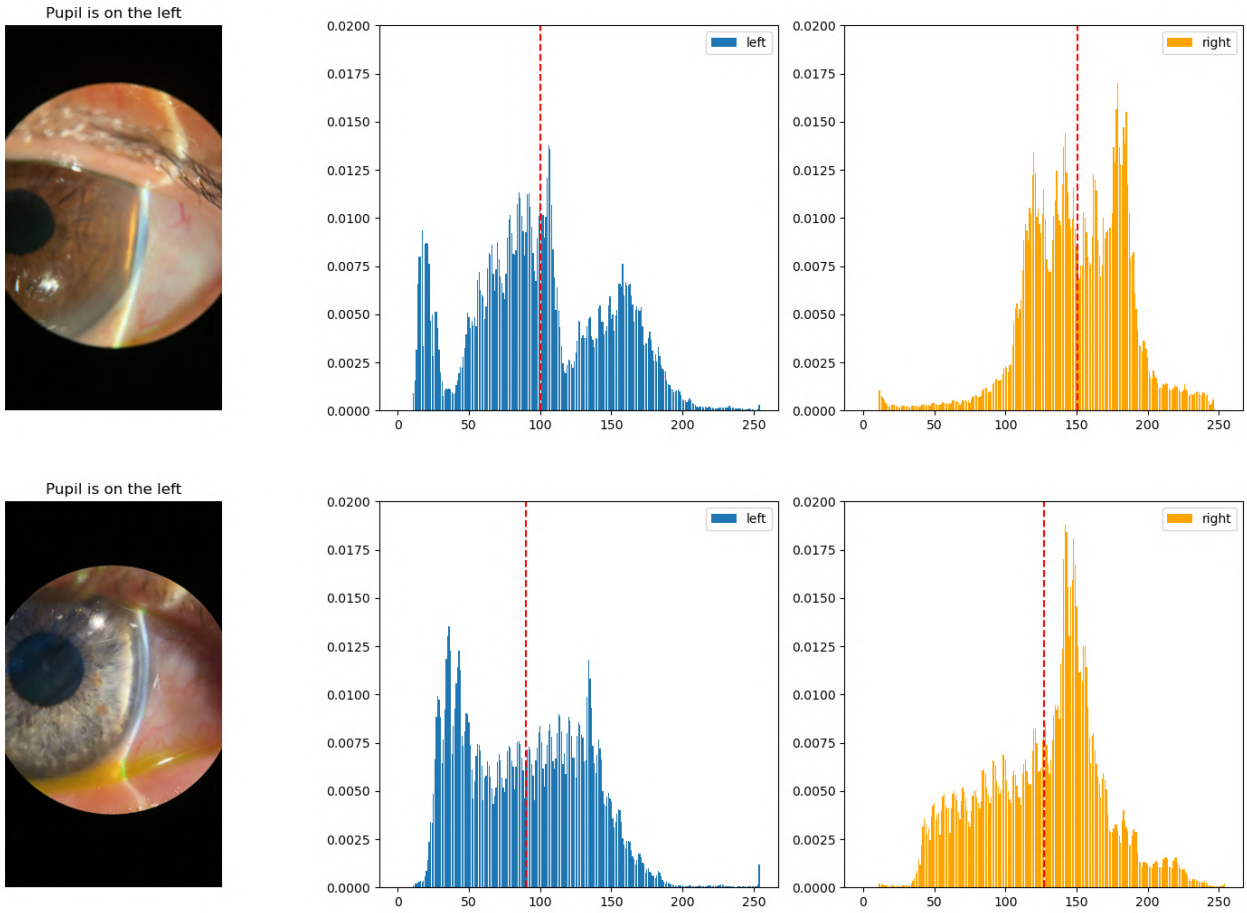

Figure 5.9 Pupil position estimation result

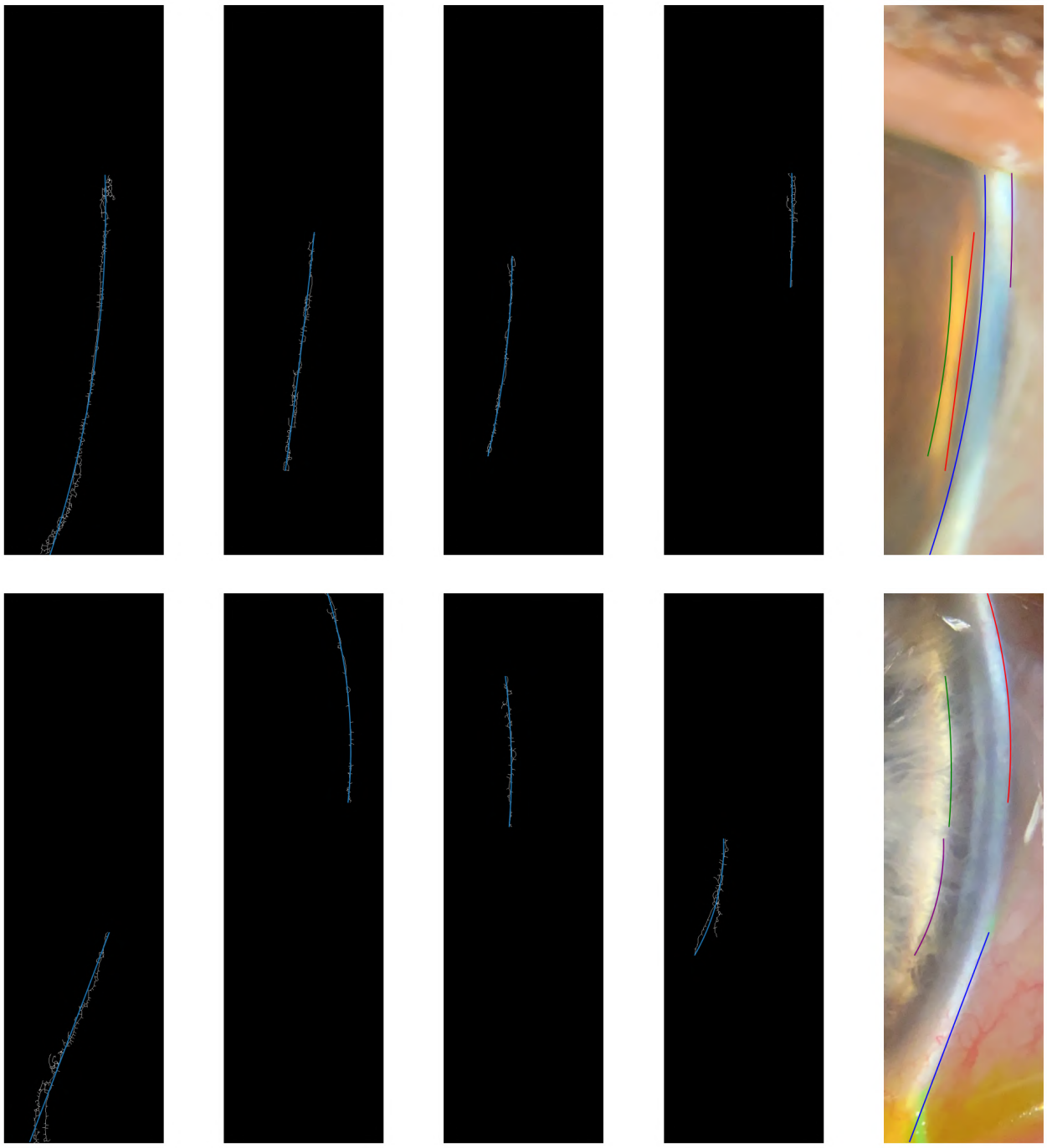

Figure 5.10 Curve fitting on the connected components

5.5 Van Herick ratio calculations

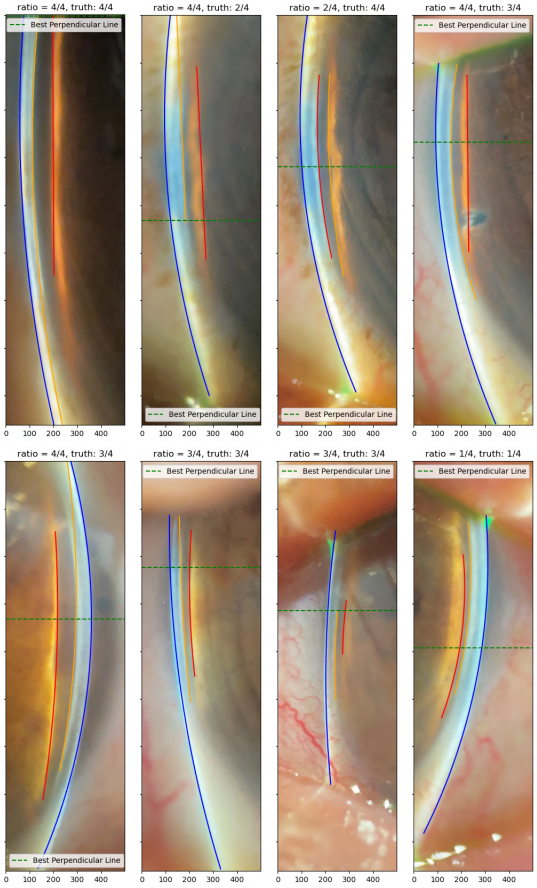

Figure 5.11 IOL ratio calculation sample results

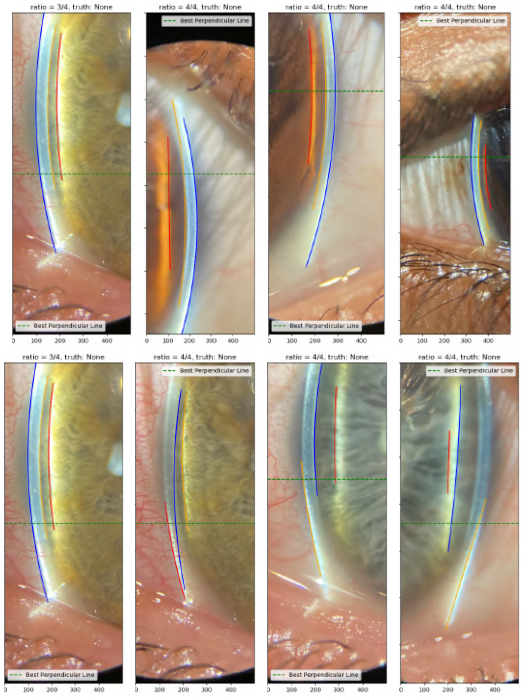

Figure 5.12 Poly ratio calculation sample results

5.6 Quantitative metric evaluation

The evaluated metrics for Van Herick classifications are accuracy, precision, recall and f1 score. The baseline for comparison is a random uniform classifier with 4 classes. Such model would have an overall accuracy of 25%, an accuracy per class of 62.5%, a precision and recall of 25% and an f1 score per class of 12.5% In this section, results will be presented first separately for the two datasets IOL and Poly respectively, then for the combination of both.

5.6.1 IOL database

The proposed method for Van Herick grading ratios was compared with expert's gradings using different scenarios. First, a multi-class evaluation produced an overall accuracy of 40%. The associated confusion matrix is presented in figure 5.13.

Achieving a 40% overall accuracy highlights the complexity and challenges inherent to this task, mostly due to the high variability in the data. While this may seem low, it represents a step forward compared to random classifier (accuracy of 25%), demonstrating the potential of the developed method. It is important to highlight that images with limitations detailed in section 5.8 were not excluded from the dataset.

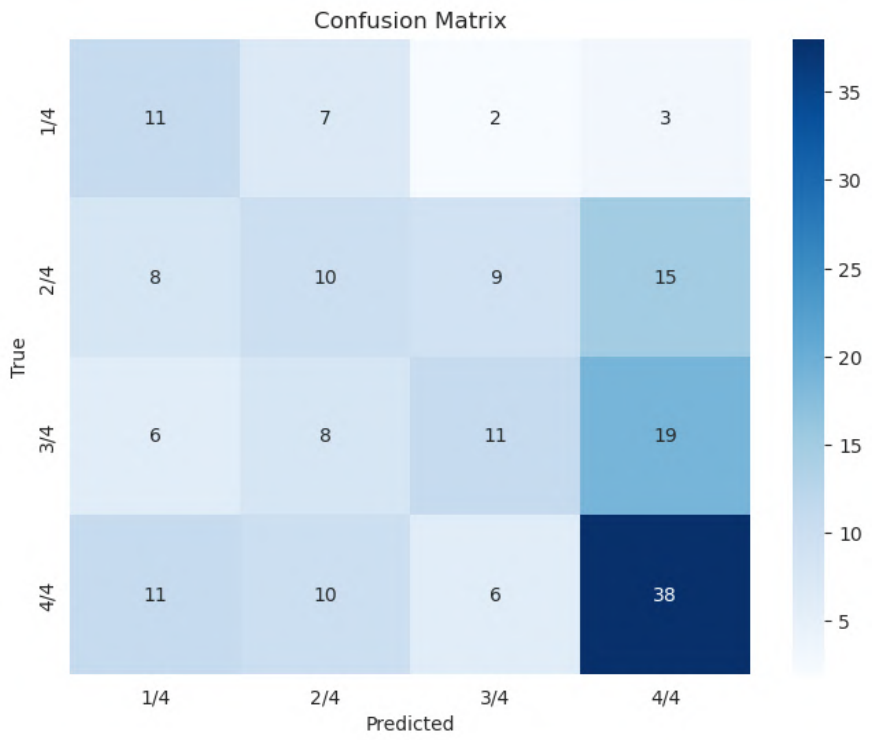

Figure 5.13 Confusion matrix for all classes in the IOL database, overall accuracy = 40%

Class	TP	FP	FN	TN	Accuracy	Precision	Recall	F1 Score
1/4	11	25	12	126	0.79	0.31	0.48	0.37
2/4	10	25	32	107	0.67	0.29	0.24	0.26
3/4	11	17	33	113	0.71	0.39	0.25	0.31
4/4	38	37	27	72	0.63	0.51	0.58	0.54

Table 5.1 Evaluation metrics for each class in the IOL database

Diving deeper into the individual classes scores from table 5.1, the open angles (4/4) have the highest F1 score. It is easier to correctly segment the light slits when the space between them is large, the merging of close elements is hence less likely. For accuracy values per class, the results for all four categories are higher than the baseline of 62.5%. The same goes for precision and F1 score. However, the recall values for ratios of 2/4 and 3/4 are similar to the baseline, showing a low sensitivity, only 24-25% of these ratios are detected. To better analyze the diagnostic performance of the algorithm, the multi-class problem was transformed into a binary classification. The scenarios were tested to analyze the ability of the proposed method to distinguish severe PACG cases, moderate cases and normal open-angle cases. The resulting scenarios are presented in table 5.2, as well as the associated evaluation metrics.

Scenario	TP	FP	FN	TN	Accuracy	Precision	Recall
1 (1/4 vs 2/4, 3/4, 4/4)	11	25	12	126	0.79	0.31	**0.48**
2 (1/4, 2/4 vs 3/4, 4/4)	36	35	29	74	0.63	0.51	0.55
3 (1/4, 2/4, 3/4 vs 4/4)	72	27	37	38	0.63	0.73	0.66

Table 5.2 Metrics for each scenario in the IOL database

In a clinical pre-screening scenario, especially for PACG detection, the recall is more important, since it represents the percentage of positive cases that are actually detected, minimizing false negatives. The baseline value for comparison with a random model being 25%, this method performs better in all scenarios. It is significantly better at identifying moderate to severe cases (scenario 2 and 3). The recall and accuracy values are also above the baseline. However, it is important to note that in the one vs all scenarios, the accuracy is artificially increased because the true negatives dominate in the numerator (see equation 4.3).

Another way to visualize the results is to plot the ROC curve, which displays the false positive rate versus the true positive rate against a random classifier. Figure 5.14 shows these curves for the scenarios. In all three plots, the curve is above the random classifier, meaning a better classification result. The optimal point that balances both metrics is shown in blue and the values are 78% 69% and 66%. Note that the most important scenario is the first one, i.e., 1/4 vs. the rest, as it characterizes severe cases. The area under the ROC curve for scenario one is the highest (0.74).

Three confusion matrices were extracted from the optimal threshold point and are shown in Figure 5.15

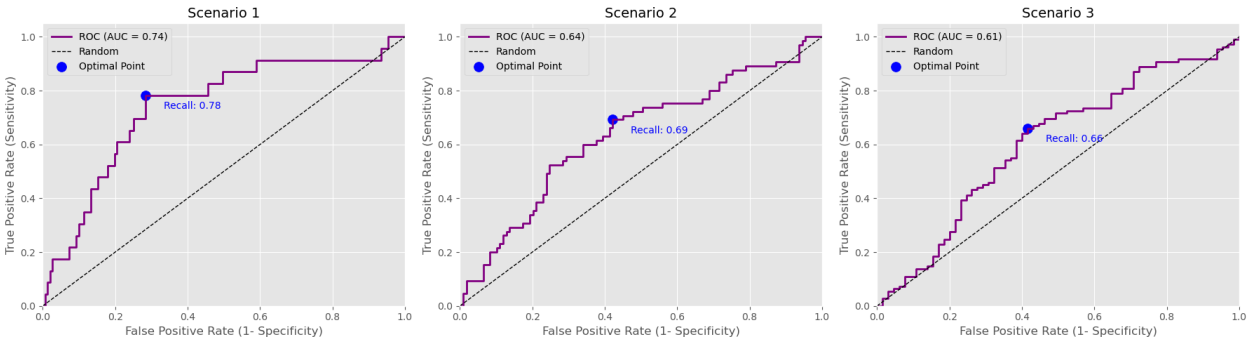

Figure 5.14 ROC curves for the binary scenarios. The recall value for the optimal point is shown in blue.

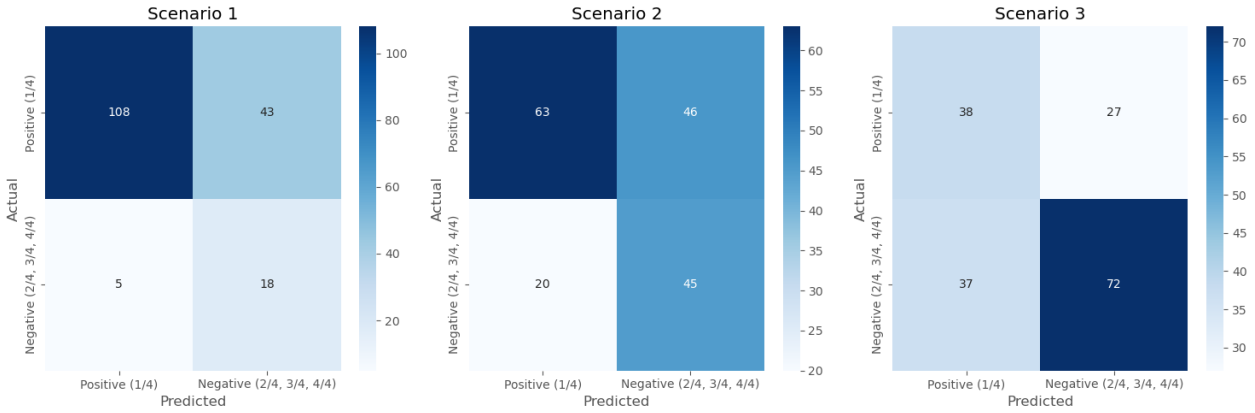

Figure 5.15 Confusion matrices for the optimal point in the binary scenarios.

In summary, the evaluation metrics on the IOL dataset are higher than the baseline, as shown by the ROC curve in Figure 5.14 as well as the area under the curve and the optimal point, reflecting the potential of the proposed method.

5.6.2 Combined databases

The combination of both datasets achieves an overall accuracy of 56%, which is significantly higher than the baseline of 25%. The combined database is also imbalanced, 76% of the images are of 4/4 open-angle. To objectively evaluate the performance on the combined database, the same grouping scenarios as the previous section were analyzed.

From table 5.4 the recall values for all scenarios are significantly higher than the baseline (25%) similarly to previous analysis, grouping severe cases with moderate cases improves the recall value, maximizes PACG detection (True positives and minimizes false negatives. As for the low precision values, it is not relevant in a clinical setting where the consequences of false negatives are more important than false positives.

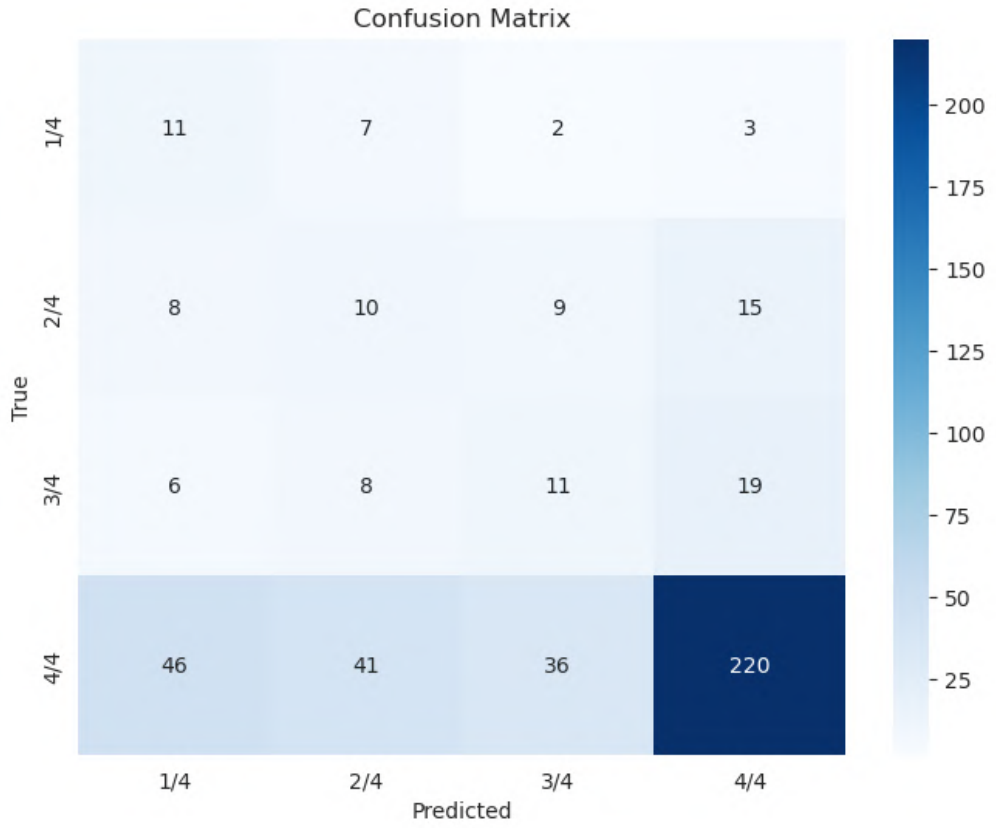

Figure 5.16 Confusion matrix for all classes in the IOL + POLY database, overall accuracy = 56%

Class	TP	FP	FN	TN	Accuracy	Precision	Recall	F1 Score
1/4	11	60	12	369	0.84	0.15	0.48	0.23
2/4	10	56	32	354	0.81	0.15	0.24	0.19
3/4	11	47	33	361	0.82	0.19	0.25	0.22
4/4	220	37	123	72	0.65	0.86	0.64	0.73

Table 5.3 Evaluation metrics for each class in the combined database

Scenario	TP	FP	FN	TN	Accuracy	Precision	Recall
1 (1/4 vs 2/4, 3/4, 4/4)	11	60	12	369	0.84	0.15	**0.48**
2 (1/4, 2/4 vs 3/4, 4/4)	36	101	29	286	0.71	0.26	**0.55**
3 (1/4, 2/4, 3/4 vs 4/4)	72	123	37	220	0.65	0.37	**0.66**

Table 5.4 Metrics for each scenario in the combined database

The ROC curves for the binary scenarios are shown in Figure 5.17. The plots show that the algorithm's performance surpasses a random classifier, with areas under the curve of 0.78, 0.68 and 0.6 for the three scenarios presented in Table 5.4. The optimal recall values are of 78%, 69% and 67% which reflects the good performance of the algorithm. The confusion matrices for the optimal threshold point are presented in Figure 5.18.

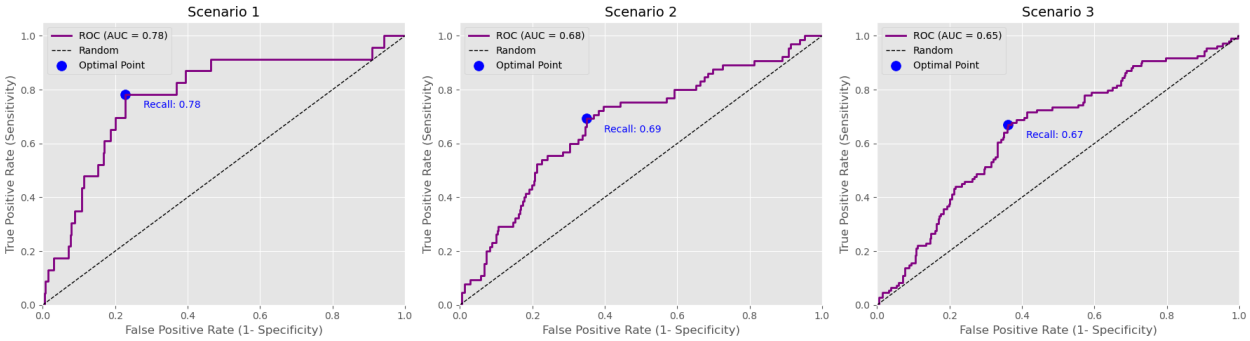

Figure 5.17 ROC curves for the binary scenarios. The recall value for the optimal point is shown in blue.

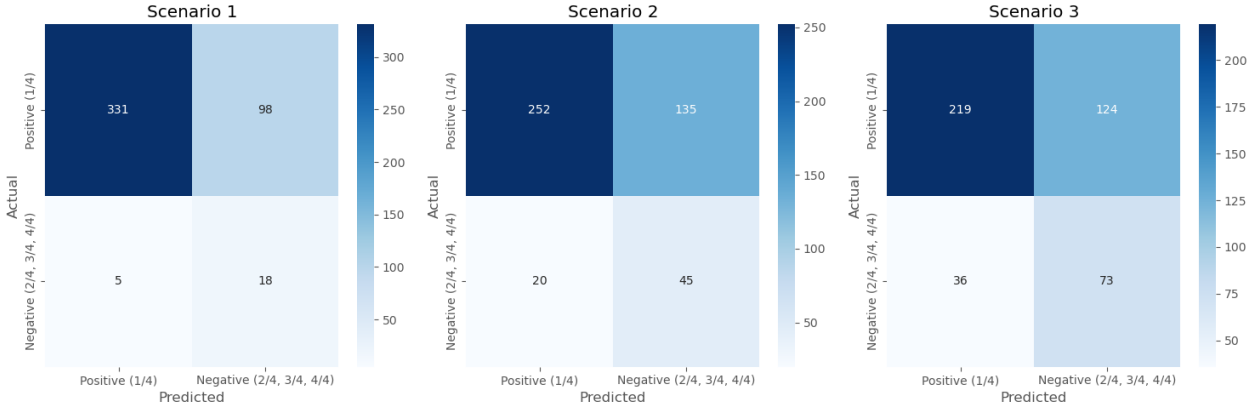

Figure 5.18 Confusion matrices for the optimal point in the binary scenarios.

5.7 Comparison with the literature

Very little research has been conducted on Van Herick images using a slit-lamp setup. Most articles cited either use supervised learning, which requires labeled data, or use different types of images, acquired with a specific setup, making it difficult to fairly compare our method with the literature. Among all previous work in our literature review, we can compare our results with [56]. They used an SVM model to predict the risk of angle closure and achieved a sensitivity of 62.5%, which is lower than our results.

5.8 Qualitative evaluation of intermediate steps for parametric curve fitting

This sections presents 6 sample cases and discusses the limitations of the proposed algorithm.

5.8.1 Horizontal line calculator limitation: invalidating correct curves

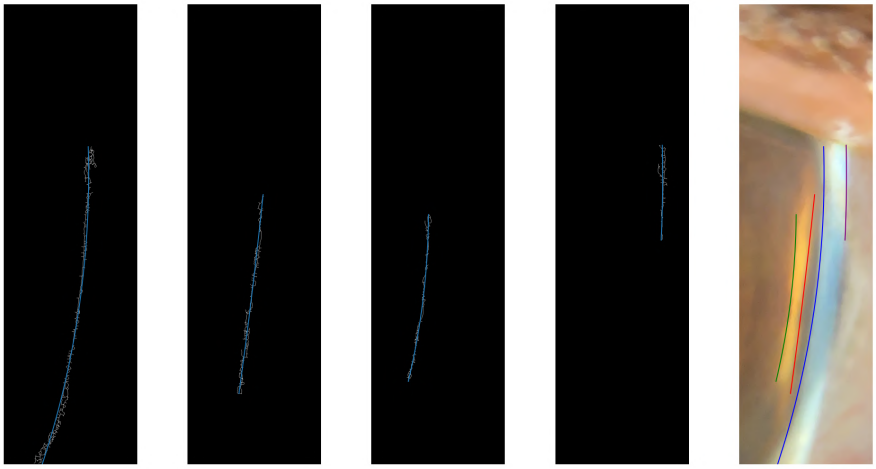

(a) Connected Component Analysis final result

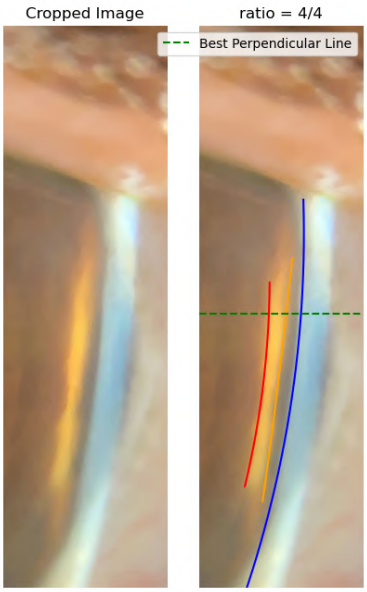

(b) Final fitted arc circles on the original image

Figure 5.19 Parametric curve fitting intermediate and final results

Figure 5.19 (a) shows a correct detection of the slit contour curves, however, in the final result, only 3 curves are displayed. This is a limitation caused by the perpendicular line calculator

that invalidate curves with abnormal tangents relative to the majority. The purple line is hence eliminated and the ratio calculation is invalid.

5.8.2 Disconnected elements

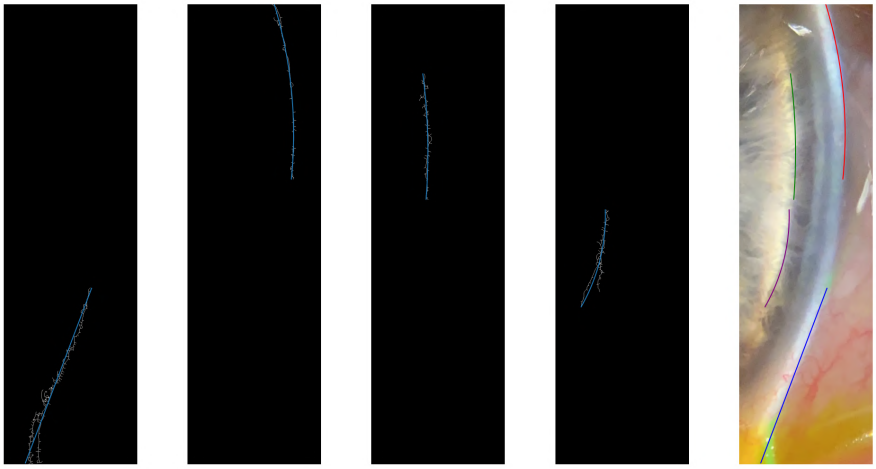

Figure 5.20 Connected Component Analysis final result

The second example illustrates the impact of disconnected arcs. The red and blue curves are too far apart to be reconnected with the correcting function. As for the green and purple curves, angles of the endpoint's tangents are too distant, which represents a limitation of the re-connecting function. This image was automatically discarded by the perpendicular computation line algorithm.

5.8.3 Poor quality binary gradient mask

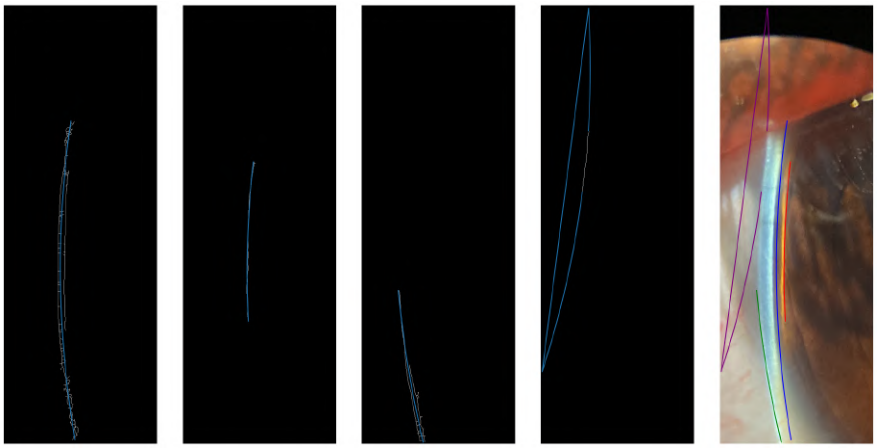

(a) Connected Component Analysis final result

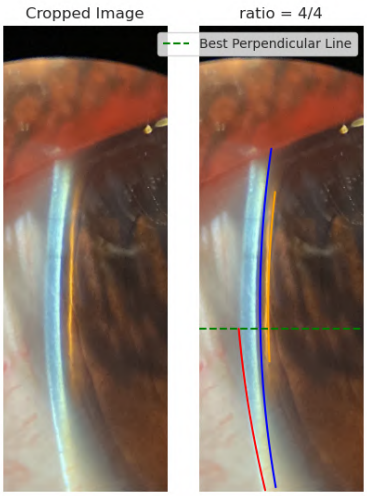

(b) Final fitted arc circles on the original image

Figure 5.21 Parametric curve fitting intermediate and final results

This case illustrates the effect of a poor quality binary skeleton mask. Figure 5.21 (a) shows double connected curves in the same element. The first 3 curves (left) are correctly fitted, unlike the last one, that detects a circular curve in the opposite direction, which explains the inversion of the starting and endpoints, since they are generated according to the curvature direction stated by the pupil position. The fallback method implemented in the computing horizontal line function eliminates this mistake by invalidating the purple curve. The final arc circle fitting in Figure 5.21 is clinically incorrect. The blue curve is not precisely on the right contour.

5.8.4 Correct results

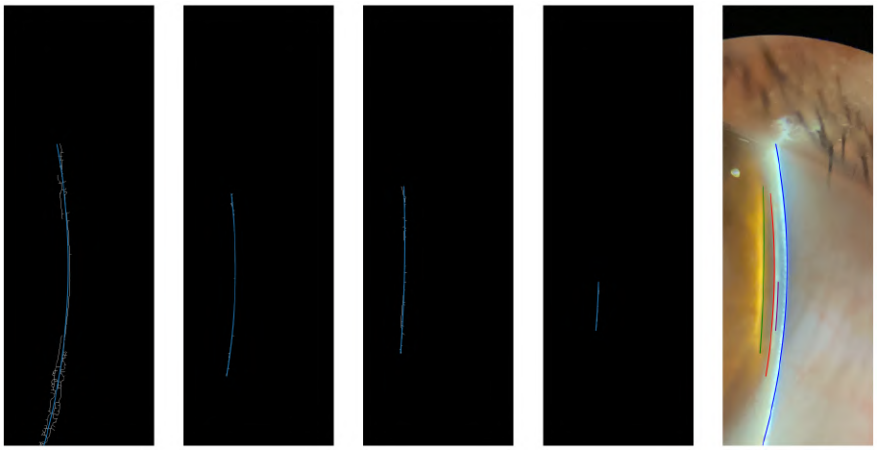

(a) Connected Component Analysis final result

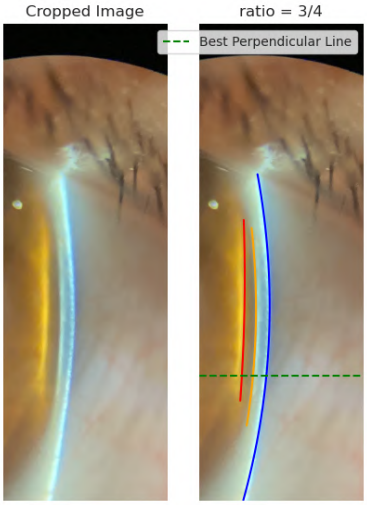

(b) Final fitted arc circles on the original image

Figure 5.22 Parametric curve fitting intermediate and final results

The example illustrated in figure 5.22 is a correct arc fitting. In a clinical context, the horizontal line should be higher, corresponding to the most convex point on the blue curve. However, this criteria was not used to determine the line position since it is highly dependent on the fitted arc position, making it sensitive to fitting mistakes.

(a) Connected Component Analysis final result

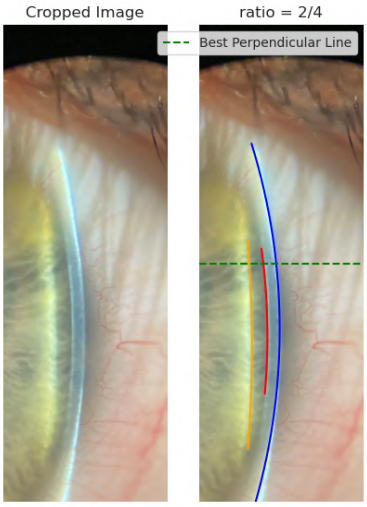

(b) Final fitted arc circles on the original image

Figure 5.23 Parametric curve fitting intermediate and final results

Figure 5.23 is a perfect example of the arc circle fitting on the Van Herick images.

5.8.5 Prominent blood vessel detection and rectangular ROI position

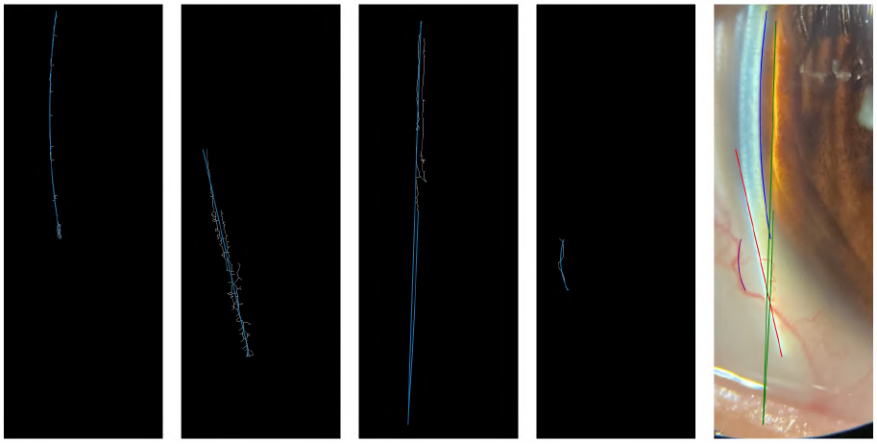

(a) Connected Component Analysis final result

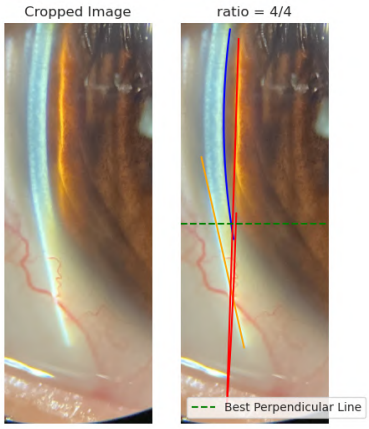

(b) Final fitted arc circles on the original image

Figure 5.24 Parametric curve fitting intermediate and final results

The final arc fitting in figure 5.23 is incorrect. Several issues can be extracted.

- Despite the visible slit and its reflection, the rectangular window is not centered around the object of interest.
- The prominent blood vessel at the lower left corner is detected bu the curve fitting function, showing the limitation of the algorithm to the presence of blood vessels.
- The green line in 5.23 (a) has inverted start and end points, which suggests that the detected arc circle has its center x-coordinate in the opposite direction, emphasizing another limitation of the algorithm.

CHAPTER 6 CONCLUSION

6.1 Summary of Works

In this work, we proposed an automatic pipeline for Van Herick ratio calculation and classification using image processing techniques to evaluate its diagnostic potential for primary angle closure glaucoma (PACG).

We first collected new anterior segment images to complement the dataset provided by our industrial partner, LightX. The proposed pipeline comprises a series of sequential processes to achieve the final classification goal without employing deep learning.

Initially, a circular ROI mask is applied to remove the background, followed by a rectangular ROI mask that targets the light slits to minimize noise caused by surrounding ocular structures during slit segmentation. Several filters and binary thresholding are then applied sequentially to isolate the structure of interest, along with a connected component analysis and an arc-fitting function to compute the distance measurements needed for Van Herick ratio computation.

The pipeline's performance was evaluated using standard metrics, including area under the ROC curve (AUC-ROC), accuracy, precision, recall, and F1 score. The results demonstrated that the pipeline outperforms a random multi-class classifier baseline model. The AUC-ROC scores for the three evaluated scenarios were 78%, 68%, and 65%, highlighting the model's ability to distinguish between classes, especially when the threshold for the binary scenario is between the most severe case (1/4) and the three other angles (2/4, 3/4 and 4/4).

However, it is important to place these results in perspective, considering the inherent variability of the analyzed images. This variability includes differences in image quality, color distribution, and challenges in focusing the slit on the structure of interest. These factors introduce additional complexity to the pipeline's performance evaluation and highlight the need for further optimization and standardization of image acquisition protocols to improve consistency and robustness. Despite these challenges, the proposed pipeline offers a practical foundation for further development and refinement in automating the Van Herick test.

6.2 Limitations

The developed pipeline for Van Herick ratio classification to detect PACG presents some limitations. Since the algorithm comprises many sequential steps, errors in intermediate

stages can propagate to the final results. Despite implementing fallback measures to enhance robustness, some issues persist.

- If the light slits are not centered within the rectangular ROI window, other ocular structures, such as a prominent blood vessels, might interfere with slit segmentation and be mistakenly detected as a light slit.
- The perpendicular line algorithm discards curves that deviate significantly in terms of tangential orientation or position. While this serves as a control mechanism to avoid invalid curves, it sometimes eliminates valid structures that should be included for measurements.
- Disconnections between elements of the same structure frequently occur. Although a corrective function was implemented to connect lines based on proximity and orientation criteria, its effectiveness is limited.
- The precision of the arc fitting step heavily depends on the quality of the binary gradient segmentation. Excess noise or outlier detection often leads to errors during arc fitting.

The pipeline relies on several parameters (e.g., thresholds, gradients) whose optimal values are challenging to determine. Fine-tuning these parameters requires extensive trial and error and may vary across datasets, potentially affecting the robustness and generalizability of the algorithm.

6.3 Key Strengths

The proposed algorithm has several strengths. It follows a modular structure, making it adaptable to various intermediate applications. Additionally, optimizing one or a few specific modules could further enhance its performance. A key advantage is that it does not require annotations, making it suitable for unsupervised learning. Moreover, the algorithm is lightweight, ensuring efficiency, and it remains interpretable, which facilitates understanding and transparency in its decision-making process.

6.4 Future Research

This work highlights the potential of classical image processing techniques for PACG risk detection by computing the ratio between light slit contours without relying on supervised learning. Optimizing the different sequential steps of the pipeline could significantly improve its performance.

Another important direction is leveraging the proposed pipeline to generate annotation masks or parameters for light slit arc fitting segmentation. While a deep learning approach could address the challenge of variability in anterior eye segment images, such a solution would require a substantial dataset with annotated images, which currently does not exist. The methodology developed in this work could be used to partially automate the annotation process, enabling the creation of a larger dataset. This would eliminate the need for entirely manual segmentation or manual fitting of arc coordinates for each structure, a highly time-consuming process. The generated annotations could then facilitate the training of a deep learning model to automatically segment the light slits and, eventually, automate the Van Herick test's image acquisition and interpretation with greater robustness to variability.

Furthermore, the Van Herick annotations obtained could be used to train a model that no longer relies on Van Herick images but rather on alternative image types with the light beam at the center, extracting the relevant angle between the slits directly from their junction.

Another promising direction is incorporating stereo image pairs to validate results, ensuring greater robustness. Additionally, correlating images from the same patient and weighting the calculated ratios accordingly could enhance patient-level classification, leading to more reliable diagnostic outcomes.

With further improvements to different parts of the proposed method and, ideally, better contrast in the images—such as images taken in the dark to enhance the light slits—it may eventually be possible to achieve sufficiently robust results to eliminate the need for gonioscopy testing altogether.

REFERENCES

[1] InnerBody, "Human nervous system anatomy," 2024, accessed: September 2024. [Online]. Available: https://www.innerbody.com/image_nerv09/nerv06.html

[2] C. Clinic, "Glaucoma," 2022. [Online]. Available: https://my.clevelandclinic.org/health/diseases/4212-glaucoma

[3] IMAIOS, "Eye anatomy," 2024, accessed: September 2024. [Online]. Available: https://www.imaios.com/en/e-anatomy/head-and-neck/eye?mic=eye-illustrations&afi=33&is=9256&il=en&l=en&ul=true

[4] H. Philippin, "The next step: detailed assessment of an adult glaucoma patient," *Community Eye Health Journal*, vol. 25, no. 79-80, pp. 66–68, 2012. [Online]. Available: https://www.cehjournal.org/article/the-next-step-detailed-assessment-of-an-adult-glaucoma-patient/

[5] S. Stevens, C. Gilbert, and N. Astbury, "How to measure intraocular pressure: applanation tonometry," *Community eye health*, vol. 20, no. 64, p. 74, 2007.

[6] S. Sreng *et al.*, "Deep learning for optic disc segmentation and glaucoma diagnosis on retinal images," *Applied Sciences*, vol. 10, no. 14, p. 4916, 2020.

[7] Centers for Disease Control and Prevention, "Why eye exams are important," 2024. [Online]. Available: https://www.cdc.gov/vision-health/about-eye-disorders/why-eye-exams-are-important.html

[8] World Health Organization, *World Report on Vision*. Geneva, Switzerland: World Health Organization, 2019, license: CC BY-NC-SA 3.0 IGO. [Online]. Available: https://www.who.int/publications/i/item/9789241516570

[9] Statistics Canada. (2022) Sociodemographic and endogenous factors associated with access to eye care in canada, 2016 to 2019. [Online]. Available: https://www150.statcan.gc.ca/n1/pub/82-003-x/2022012/article/00003-eng.htm

[10] Space Coast Ophthalmology, "The importance of early detection in eye diseases," 2023. [Online]. Available: https://spacecoastophthalmology.com/early-detection-in-eye-diseases/

[11] H. Jayaram *et al.*, "Glaucoma: now and beyond," *The Lancet*, vol. 402, no. 10414, pp. 1788–1801, 2023. [Online]. Available: https://www.sciencedirect.com/science/article/pii/S0140673623012898

[12] National Eye Institute. (2024) Types of glaucoma. Accessed: 2024-08-19. [Online]. Available: https://www.nei.nih.gov/learn-about-eye-health/eye-conditions-and-diseases/glaucoma/types-glaucoma

[13] Centers for Disease Control and Prevention (CDC). (2024) What is glaucoma? Accessed: 2024-08-19. [Online]. Available: https://www.cdc.gov/vision-health/about-eye-disorders/glaucoma.html

[14] Moorfields eye charity | innovating glaucoma care. [Online]. Available: https://moorfieldseyecharity.org.uk/projects-we-fund/innovating-glaucoma-care

[15] N. Zhang *et al.*, "Prevalence of primary angle closure glaucoma in the last 20 years: A meta-analysis and systematic review," *Frontiers in Medicine*, vol. 7, p. 624179, 2021, accessed: 2024-08-19. [Online]. Available: https://www.frontiersin.org/articles/10.3389/fmed.2020.624179/full

[16] H. Jayaram *et al.*, "Glaucoma: now and beyond," *The Lancet*, vol. 402, no. 10414, pp. 1788–1801, 2023.

[17] N. Gupta and Y. M. Buys, *Glaucoma Diagnosis and Management*. StatPearls Publishing, 2023, ch. Glaucoma Diagnosis and Management, accessed: 2024-08-14. [Online]. Available: https://www.ncbi.nlm.nih.gov/books/NBK541069/

[18] K. Kashiwagi *et al.*, "Usefulness of peripheral anterior chamber depth assessment in glaucoma screening," *Eye*, vol. 19, no. 9, pp. 990–994, 2005.

[19] N. S. Choudhari *et al.*, "Diagnostic accuracy of van herick technique to detect pre-disease states of primary angle closure glaucoma in a resource constraint region," *Ophthalmic epidemiology*, vol. 26, no. 3, pp. 175–182, 2019.

[20] American Academy of Ophthalmology, "Parts of the eye: Anatomy," 2024, accessed: 2024-12-09. [Online]. Available: https://www.aao.org/eye-health/anatomy/parts-of-eye

[21] D. K. Sunderland and A. Sapra, *Physiology, Aqueous Humor Circulation*. Treasure Island (FL): StatPearls Publishing, 2023.

[22] R. Machiele *et al.*, "Intraocular pressure," *StatPearls Publishing*, nov 2024. [Online]. Available: https://www.ncbi.nlm.nih.gov/books/NBK532237/

[23] J. Bader, M. Zeppieri, and S. Havens, "Tonometry," *StatPearls*, 2023.

[24] IMAIOS. (2024) Retinal ganglion cell - E-Anatomy. Accessed: 2024-09-05. [Online]. Available: https://www.imaios.com/en/e-anatomy/anatomical-structure/retinal-ganglion-cell-133706276

[25] ——, "Rod cell," https://www.imaios.com/en/e-anatomy/anatomical-structure/rod-cell-133706244, 2024, accessed: 2024-09-05.

[26] (2023) Cone cell - anatomical structure. IMAIOS. Accessed: 2024-09-05. [Online]. Available: https://www.imaios.com/en/e-anatomy/anatomical-structure/cone-cell-133706252

[27] S. Hattar *et al.*, "The role of melanopsin in regulating circadian rhythms, sleep, and pupillary light reflexes," *eLife*, vol. 10, p. e68903, 2021. [Online]. Available: https://elifesciences.org/articles/68903

[28] J. H. Kang *et al.*, "Biomarkers of glaucoma: Current perspectives and future directions," *The Lancet Regional Health – Americas*, vol. 21, p. 100195, 2023. [Online]. Available: https://www.sciencedirect.com/science/article/pii/S2666469023000192

[29] A. K. Schuster *et al.*, "The diagnosis and treatment of glaucoma," *Dtsch Arztebl Int*, vol. 117, no. 13, pp. 225–234, 2020.

[30] S. J. Gedde *et al.*, "Primary angle-closure disease preferred practice pattern®," *Ophthalmology*, vol. 128, no. 1, pp. P30–P70, 2021. [Online]. Available: https://www.sciencedirect.com/science/article/pii/S016164202031023X

[31] ——, "Primary angle-closure disease preferred practice pattern®," *Ophthalmology*, vol. 128, no. 1, p. P30–P70, Jan. 2021. [Online]. Available: http://dx.doi.org/10.1016/j.ophtha.2020.10.021

[32] X. Sun *et al.*, "Primary angle closure glaucoma: what we know and what we don't know," *Progress in retinal and eye research*, vol. 57, pp. 26–45, 2017.

[33] J. Y. Lee, Y. Y. Kim, and H. R. Jung, "Distribution and characteristics of peripheral anterior synechiae in primary angle-closure glaucoma," *Korean Journal of Ophthalmology*, vol. 20, no. 2, p. 104, 2006. [Online]. Available: http://dx.doi.org/10.3341/kjo.2006.20.2.104

[34] E. Han, A. E. Levitt, and R. K. Lee, "Community vision screening," Feb. 2019. [Online]. Available: https://glaucomatoday.com/articles/2019-jan-feb/community-vision-screening

[35] J. D. Stein, A. P. Khawaja, and J. S. Weizer, "Glaucoma in adults—screening, diagnosis, and management: A review," *JAMA*, vol. 325, no. 2, p. 164, Jan. 2021. [Online]. Available: http://dx.doi.org/10.1001/jama.2020.21899

[36] L. M. Khazaeni, "Examen du patient en ophtalmologie," Apr. 2022. [Online]. Available: https://www.merckmanuals.com/fr-ca/professional/troubles-oculaires/prise-en-charge-du-patient-souffrant-de-troubles-ophtalmologiques/examen-du-patient-en-ophtalmologie

[37] I. Riva *et al.*, "Anterior chamber angle assessment techniques: A review," *Journal of Clinical Medicine*, vol. 9, no. 12, 2020. [Online]. Available: https://www.mdpi.com/2077-0383/9/12/3814

[38] A. G. Konstas *et al.*, "Diurnal and 24-h intraocular pressures in glaucoma: Monitoring strategies and impact on prognosis and treatment," 2018. [Online]. Available: https://adisjournals.figshare.com/articles/Diurnal_and_24-Hour_Intraocular_Pressures_in_Glaucoma_Monitoring_Strategies_and_Impact_on_Prognosis_and_Treatment/7165489

[39] R. R. S. R. A. M. Ricardo Alexandre Stock, Carine Ströher and E. L. Bonamigo, "A comparative study between the goldmann applanation tonometer and the non-contact air-puff tonometer (huvitz hnt 7000) in normal eyes," *Clinical Ophthalmology*, vol. 15, pp. 445–451, 2021. [Online]. Available: https://www.tandfonline.com/doi/abs/10.2147/OPTH.S294710

[40] D. Laroche *et al.*, "Preventing blindness from glaucoma with patient education, the nidek gs-1 gonioscope, lensectomy and microinvasive glaucoma surgery," *Journal of the National Medical Association*, vol. 115, no. 2, p. 175–185, Apr. 2023. [Online]. Available: http://dx.doi.org/10.1016/j.jnma.2023.01.014

[41] W. Nolan and A. Onakoya, "Compétences et techniques de gonioscopie," *Revue de Santé Oculaire Communautaire*, vol. 19, no. 27, pp. 10–12, 2022. [Online]. Available: https://www.cehjournal.org/article/competences-et-techniques-de-gonioscopie/

[42] P. Ma *et al.*, "Evaluation of the diagnostic performance of swept-source anterior segment optical coherence tomography in primary angle closure disease," *American*

Journal of Ophthalmology, vol. 233, p. 68–77, jan 2022. [Online]. Available: http://dx.doi.org/10.1016/j.ajo.2021.06.033

[43] H. Hao *et al.*, "Angle-closure assessment in anterior segment oct images via deep learning," *Medical Image Analysis*, vol. 69, p. 101956, 2021.

[44] M. N. Zahoor and M. M. Fraz, "Fast optic disc segmentation in retina using polar transform," *IEEE Access*, vol. 5, pp. 12 293–12 300, 2017.

[45] H. Raja *et al.*, "Glaucoma detection using optical coherence tomography images: a systematic review of clinical and automated studies," *IETE Journal of Research*, vol. 69, no. 11, pp. 7958–7978, 2023.

[46] N. A. Mohamed *et al.*, "An automated glaucoma screening system using cup-to-disc ratio via simple linear iterative clustering superpixel approach," *Biomedical Signal Processing and Control*, vol. 53, p. 101454, 2019.

[47] A. Geevarghese *et al.*, "Optical coherence tomography and glaucoma," *Annual review of vision science*, vol. 7, no. 1, pp. 693–726, 2021.

[48] G. Song *et al.*, "A review of low-cost and portable optical coherence tomography," *Progress in Biomedical Engineering*, vol. 3, no. 3, p. 032002, May 2021. [Online]. Available: http://dx.doi.org/10.1088/2516-1091/abfeb7

[49] D. Turbert, "Visual field test," *Americal Academy of Ophtalmology*, mar 2022. [Online]. Available: https://www.aao.org/eye-health/tips-prevention/visual-field-testing

[50] C. Clinic, "Visual field test," apr 2023. [Online]. Available: https://my.clevelandclinic.org/health/diagnostics/14420-visual-field-test

[51] Y. Ou, "Glaucoma: Understanding the visual field test | brightfocus foundation," jul 2021. [Online]. Available: https://www.brightfocus.org/glaucoma/article/glaucoma-understanding-visual-field-test

[52] S. Ruia and K. Tripathy, "Humphrey visual field," *StatPearls Publishing*, aug 2023. [Online]. Available: https://www.ncbi.nlm.nih.gov/books/NBK585112/

[53] T. Fedullo *et al.*, "A machine learning approach for a vision-based van-herick measurement system," in *2021 IEEE International Instrumentation and Measurement Technology Conference (I2MTC)*. IEEE, 2021, pp. 1–6.

[54] ——, "Assessment of a vision-based technique for an automatic van herick measurement system," *IEEE Transactions on Instrumentation and Measurement*, vol. 71, pp. 1–11, 2022.

[55] D. Cassanelli *et al.*, "Training of an artificial intelligence algorithm for automatic detection of the van herick grade," in *Ophthalmic Technologies XXXII*, D. X. Hammer, K. M. Joos, and D. V. Palanker, Eds. SPIE, mar 2022, p. 61. [Online]. Available: http://dx.doi.org/10.1117/12.2607610

[56] ——, "Image analysis algorithm for the anterior chamber angle closure estimation and van herick classification," in *2023 9th International Workshop on Advances in Sensors and Interfaces (IWASI)*, 2023, pp. 267–272.

[57] C. Theeraworn *et al.*, "Automatic screening of narrow anterior chamber angle and angle-closure glaucoma based on slit-lamp image analysis by using support vector machine," in *2013 35th Annual International Conference of the IEEE Engineering in Medicine and Biology Society (EMBC)*. IEEE, 2013, pp. 5887–5890.

[58] B. Babenko *et al.*, "Detection of signs of disease in external photographs of the eyes via deep learning," *Nature biomedical engineering*, vol. 6, no. 12, pp. 1370–1383, 2022.

[59] C. Qian *et al.*, "Smartphone-acquired anterior segment images for deep learning prediction of anterior chamber depth: A proof-of-concept study," *Frontiers in Medicine*, vol. 9, p. 912214, 2022.

[60] E. Shimizu *et al.*, "The use of artificial intelligence for estimating anterior chamber depth from slit-lamp images developed using anterior-segment optical coherence tomography," *Bioengineering*, vol. 11, no. 10, p. 1005, Oct. 2024. [Online]. Available: http://dx.doi.org/10.3390/bioengineering11101005

[61] D. Chen *et al.*, "Machine learning-guided prediction of central anterior chamber depth using slit lamp images from a portable smartphone device," *Biosensors*, vol. 11, no. 6, p. 182, Jun. 2021. [Online]. Available: http://dx.doi.org/10.3390/bios11060182

[62] J. Randhawa *et al.*, "Generalisability and performance of an oct-based deep learning classifier for community-based and hospital-based detection of gonioscopic angle closure," *British Journal of Ophthalmology*, vol. 107, no. 4, pp. 511–517, 2023.

[63] B. Y. Xu *et al.*, "Deep learning classifiers for automated detection of gonioscopic angle closure based on anterior segment oct images," *American Journal of Ophthalmology*,

vol. 208, pp. 273–280, 2019. [Online]. Available: https://www.sciencedirect.com/science/article/pii/S0002939419303940

[64] H. Fu *et al.*, "Disc-aware ensemble network for glaucoma screening from fundus image," *IEEE transactions on medical imaging*, vol. 37, no. 11, pp. 2493–2501, 2018.

[65] ——, "Joint optic disc and cup segmentation based on multi-label deep network and polar transformation," *IEEE transactions on medical imaging*, vol. 37, no. 7, pp. 1597–1605, 2018.

[66] A. Neto *et al.*, "Optic disc and cup segmentations for glaucoma assessment using cup-to-disc ratio," *Procedia Computer Science*, vol. 196, pp. 485–492, 2022.

[67] C. P. Bragança *et al.*, "Detection of glaucoma on fundus images using deep learning on a new image set obtained with a smartphone and handheld ophthalmoscope," in *Healthcare*, vol. 10, no. 12. MDPI, 2022, p. 2345.

[68] F. Girard *et al.*, "Atlas-based score for automatic glaucoma risk stratification," *Computerized Medical Imaging and Graphics*, vol. 87, p. 101797, jan 2021. [Online]. Available: http://dx.doi.org/10.1016/j.compmedimag.2020.101797

[69] Wikipedia contributors, "Color space — Wikipedia, The Free Encyclopedia," 2024, accessed: 2024-12-13. [Online]. Available: https://en.wikipedia.org/wiki/Color_space

[70] Santa Barbara City College, "Digital Video: Basic Principles," 2024, accessed: 2024-12-13. [Online]. Available: https://soma.sbcc.edu/users/davega/FILMPRO_114_EDITING_I/FILMPRO_114_04_Reference_Notes/FILMPRO_114_Digital_Video/DigitalVideo_Basic_Principles.pdf

[71] OpenCV, "Hough line transform — opencv documentation," 2024, accessed: 2024-12-09. [Online]. Available: https://docs.opencv.org/3.4/d9/db0/tutorial_hough_lines.html

[72] OpenCV contributors, "Core Array Operations — OpenCV Documentation," https://docs.opencv.org/4.x/d2/de8/group___core___array.html#ga87eef7ee3970f86906d69a92cbf064bd, 2024, [Online; accessed 13-Dec-2024].

APPENDIX A PRELIMINARY RESULTS: CIRCULAR ROI SEGMENTATION

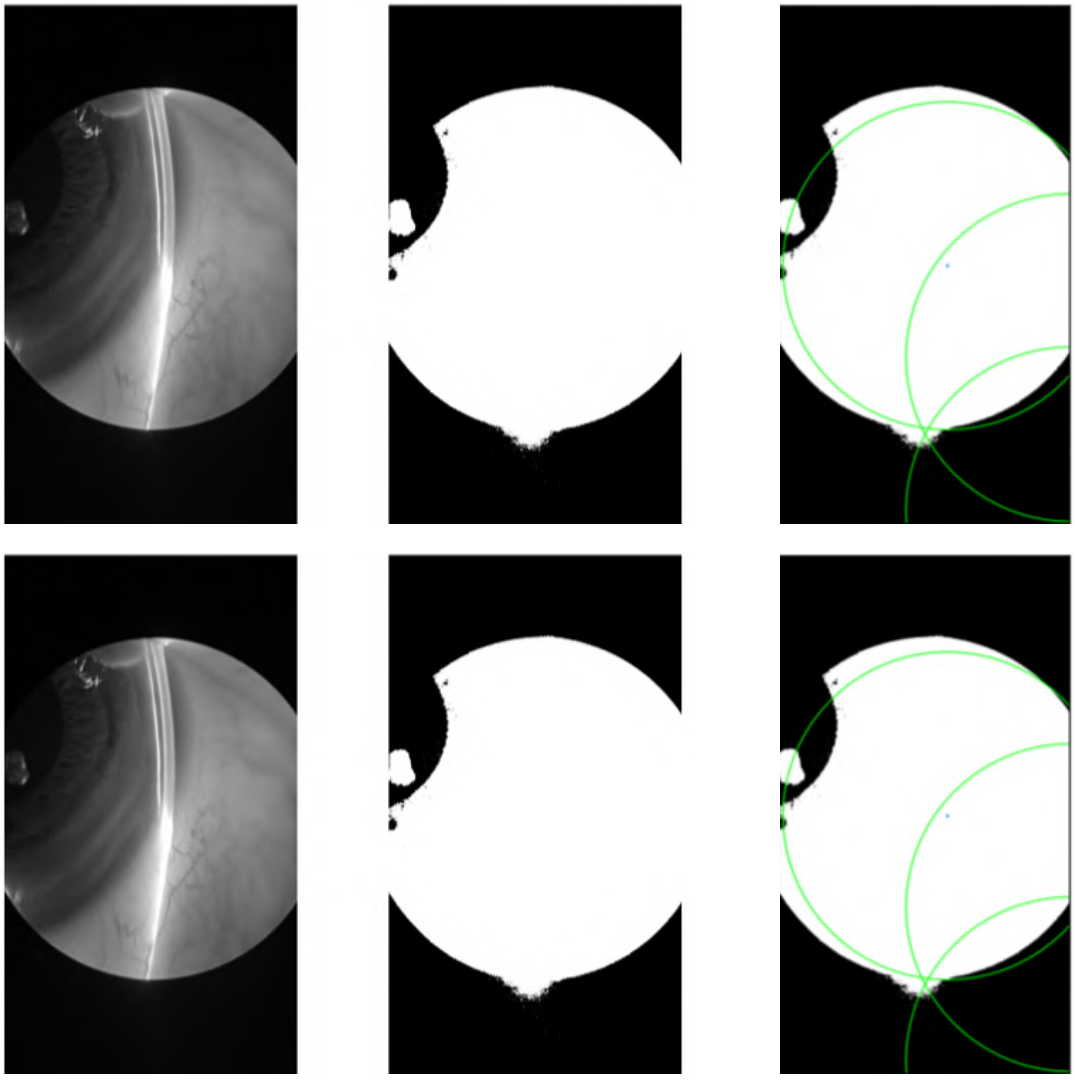

Figure A.1 Preliminary Results: Circular ROI mask. From left to right: original image, binary threshold, hough transform.

APPENDIX B EXPERIMENTAL RESULTS FOR SLIT DETECTION

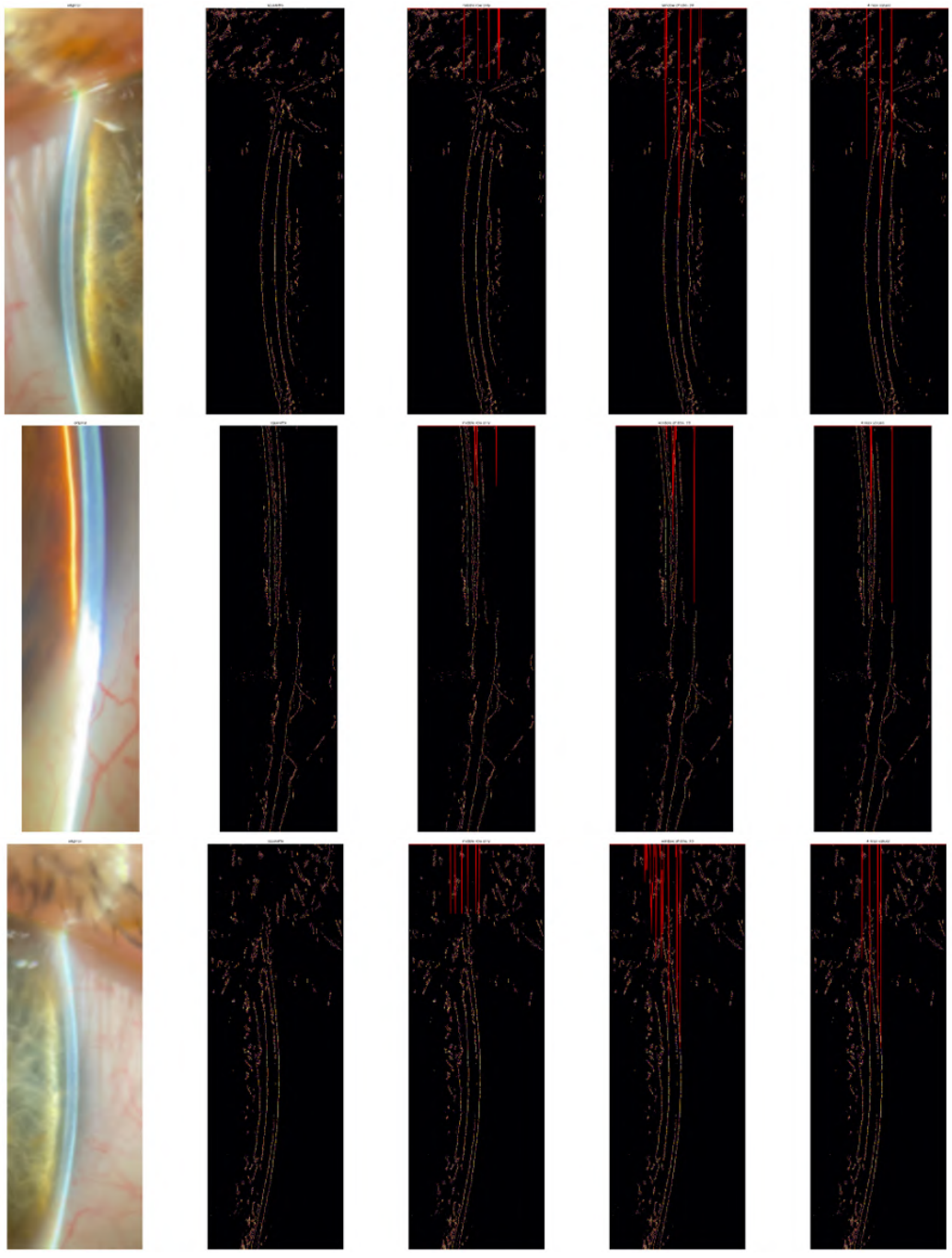

Figure B.1 Inconclusive experiment for slit measurements

APPENDIX C INFORMATION AND CONSENT FORM

Information and consent form

Title of the research activity:
Automatic Analysis of Anterior Eye Segment Images Using Deep Learning

Research team:

Persons in charge of the research activity:
Doha Zrouki
Master student
Polytechnique Montréal – GIGL department
Email: doha.zrouki@polymtl.ca

Philippe Baumstimler
Master student
Polytechnique Montréal – GIGL department
Email: philippe.baumstimler@polymtl.ca

Under the supervision of:
Lama Séoud
Supervising professor
Polytechnique Montréal – GIGL department
Email: lama.seoud@polymtl.ca

Funding of the research activity:

The present research activity is funded by MITACS, a non-profit federal research agency, in partnership with the company LightX Innovations. This company provides a mobile software application for taking anterior eye segment images and is developing artificial intelligence algorithms to analyse these images.

Conflicts of interest

Depending on the results, the advancements and improvements stemming from our research could be used by the industrial partner for commercial purposes. The collected data will be used for training pathology detection algorithms, the latter (but not the data) being subject to commercialization.

The interests of Polytechnique lie in the training of highly qualified personnel and in the advancement of knowledge. Neither the research team nor Polytechnique will receive royalties in the event of commercialization of the algorithms by the industrial partner.

Foreword

We invite you to participate in a research activity to evaluate the diagnostic power of anterior eye segment images using machine learning in order to help medical professionals in ophthalmology.

However, before accepting to participate and signing this information and consent form, please take the time to read all the information presented in it.

If you agree to participate in this research activity, our research partner will ask you to sign a separate information and consent form. This second document concerns the collection by the company of de-identified images for research purposes (other than the present project). Management of the data collected by the industrial partner will be carried out under the terms established in their consent form, Polytechnique Montréal having no authority over the latter. This second form is optional: if you do not consent to the company's terms, you can still participate in this research activity provided that you sign the present information and consent form.

We invite you to ask any questions you may have to the person in charge of the research activity or to any other research team member. If any particular word or piece of information is unclear, they can provide further explanations. We also invite you to seek advice from anyone else you wish to consult regarding your potential participation.

Présentation générale du projet de recherche

Recent research shows that it is possible to detect signs of disease conditions such as diabetic retinopathy from external images of the ocular globe. These images have the advantage of being captured using standard cameras, without the need to dilate the pupil, unlike fundus images to capture the retina.

The aim of our project is to evaluate the diagnostic power of images of the anterior portion of the eye, for glaucoma in particular and more broadly for ocular pathologies. To this end, we are exploiting our industrial partner's database of ocular globe images to develop pathology detection algorithms using machine learning methods. However, this database contains very little data from subjects with no ocular pathology, and this is an obstacle to our research. This is why we want to build a "normative" database comprising images acquired from so-called "healthy" people, i.e. with no known ocular pathology, and from which we will build training, validation and test sets for our algorithms. These sets will be used to train and evaluate deep neural networks to classify images according to the associated diagnosis and to recognize images presenting diseases.

The main objectives of our study are as follows:

- Develop tools to automatically analyze images of the external ocular globe and detect the presence of PACS (Primary Angle Closure Suspect), an early sign of glaucoma;

- Develop tools for detecting anomalies in external ocular globe images.

In the longer term, our research could enhance the accessibility of ophthalmological diagnosis, for example using slit lamp images in optometry clinics or via remote patient monitoring.

In order to reach our objectives, we aim to recruit 100 participants for a data collection campaign using slit-lamp examination. A series of tests will be carried out by an ophthalmologist and each test will result in a pair of stereoscopic photos (one for each eye). Only your eyes will be photographed. In addition to the images acquired, we will ask you to provide us with the following information:

- Age
- Sex
- Ethnic origin
- Optical correction (if known)

This information is only collected for sensitivity analysis of our machine learning models and will not be shared with anyone outside the research team.

Inclusion/exclusion criteria

For this activity, we are looking for people of legal age and of all genders and backgrounds who are able to give their consent, speak French or English, and are sighted. You **cannot** participate in this activity if you have, or have had, any of the following conditions:

- Glaucoma
- Diabetic retinopathy
- Macular degeneration
- Cataracts.

Nature and duration of your participation in the research activity

Your participation in the research activity will take the form of ophthalmic image acquisition using a device called a slit lamp, which will be operated by an ophthalmologist. A pair of stereoscopic images of each eye will be acquired in 7 different light configurations, each one allowing visualization of a specific part of the eye (conjunctiva, cornea, iris, crystalline lens, anterior chamber and vitreous humor). In all, 28 images will be collected per participant. The entire acquisition procedure will take between 5 and 10 minutes.

Additional information about you (age, sex, ethnicity, optical correction if known) will be collected by the research team for model sensitivity analysis.

Risks that may arise from your participation in the research activity

The present activity should not entail any risks greater than those encountered in your everyday life. Handling of the acquisition device will be carried out entirely by an expert in the medical field (an experienced ophthalmologist), and does not require the administration

of eye drops. The eye tests use only light in the visible spectrum, thus some discomfort associated with illumination may be experienced.

Possible drawbacks of participating in the study

The drawbacks of participating in the research are the time required for the acquisitions (maximum 10 minutes), transportation to the laboratory where the acquisitions will take place, and possible discomfort caused by illumination from the slit lamp. In addition, people wearing contact lenses will need to remove them for the duration of the session.

Possible benefits of participating in the study

Your participation in the study will enable you to have your eyes tested by an ophthalmologist, who will be able to tell you if any abnormalities are observed.

Incidental findings:

In the event that any sign of pathology is discovered during acquisition, the ophthalmologist will be able to communicate this to the participant and refer them to their attending physician. However, the potential detection of signs of pathology after image collection (resulting from algorithms developed by the research team) will not be communicated to participants, by virtue of the trust placed in the health professional's assessment during data acquisition.

Financial compensation

You will receive financial compensation of $20 for your time.

Compensation in the event of harm and participants' rights

Should you suffer any harm whatsoever as a result of your participation in this research activity, you do not waive any of your rights or release the researchers, the funding organization or Polytechnique Montréal from their legal and professional responsibilities.

Voluntary participation and possibility of withdrawal:

Your participation in this research activity is voluntary. You are therefore free to refuse to participate and can decide to withdraw your consent at any time without having to justify your decision or risk any harm. In that case, you only need to inform the research team's contact person by giving them verbal notice.

In the event of withdrawal, you may request that your data be deleted. However, it will not be possible to withdraw your data or material from any analyses carried out once these have been published or distributed. The financial compensation may be kept by the participant after withdrawal.

Throughout the research process, and with your consent, you will receive timely information relevant to your participation.

The research team will ensure that the consent process is properly established in a private and non-coercive setting.

The research team and the research ethics committee reserve the right to remove you from the study if you fail to comply with any guidelines provided, if there are administrative reasons to abandon the activity, if your participation is no longer safe or for any other reason concerning the feasibility of the study. Should such a situation arise, the research team will inform you as soon as possible.

Confidentiality and protection of your data

The research team will collect and record all your data (images and demographic information) in a secure manner and in such a way as to protect its confidentiality.

Here is how we will protect your data **during collection**:

- Your information will be de-identified and an identification key linking your data to your first and last name will be kept only by the researcher in charge of this project.
- The identification key will only be used to trace your data and delete it should you withdraw your consent.
- De-identified data will be stored on a hard disk with an encryption key belonging to the research team.

Here is how we will protect your data **during analyses and transfer between team members:**

- Information collected from participants will remain confidential and will not be shared with anyone outside the research team.
- Demographic information will only be used for model sensitivity analysis and statistics.
- Data will be shared on secure platforms or by external hard disk with encryption key.
- Data may be copied to the local hard disk of research laboratory computers during training and model validation but will be completely deleted once these phases are completed.

Here is how we will protect your data **in publications**:

- Data will be de-identified, and no mention of participants' identity or contact details will be made in any publications.
- The images include only one eye at a time and exclude the rest of the face; it will therefore be impossible to trace the participant's identity from them.

Finally, here is how we will protect your data **after completion of the research project**:

- Your data will be stored on an encrypted hard disk held by the researcher in charge of the project, Professor Lama Séoud, for a period of 10 years after the end of this research project, in accordance with professional standards of practice.

You have the right to consult your research file to verify the accuracy of the information collected for as long as the research team or Polytechnique Montréal holds this information.

However, in order to preserve the scientific integrity of the research project, certain information will be available only at the end of the research project.

Publication of research results

The research work carried out in the context of this project and using the data collected may be published in academic theses and in scientific journals, or presented at scientific conferences. Participants will be informed by e-mail of the publications and presentations arising from the study, provided that they agree to be contacted for this purpose.

Contact persons

If you have any questions about the **scientific aspects** of the research project, or if you wish to **withdraw from the study**, you can contact supervising professor Lama Seoud by e-mail at lama.seoud@polymtl.ca.

For any concerns about your rights or about the research team's responsibilities regarding your participation in this project, you can contact Polytechnique Montréal's Research Ethics Board at (514) 340-4711, ext. 4420, or by e-mail at ethique@polymtl.ca.

Consent to participation in the research activity

1. I have read the information and consent form, which describes the nature and the conduct of the research project along with the risks and drawbacks that may arise.
2. I understand that I have the right to receive adequate answers to any questions about my involvement in this project that I may ask at any time during my participation.
3. I hereby consent to participate freely in this project, having taken as much time as I needed to think about it and without having been pressured to do so.
4. I understand that by participating in this research project, I neither waive any of my rights, nor release the researchers from their responsibilities.
5. I understand that I can consult the file that the research team will keep about me.
6. At any time, by simple notice on my part, I can reconsider my decision to participate and will then be immediately released from my involvement.
7. I have received a copy of this document.
8. I hereby consent to give the following information about myself, provided that it remains anonymous: age, sex, ethnicity and optical correction (if known).
9. I hereby consent to the training of machine learning algorithms using photos of my eyes and labelling of the anonymized data.
10. I hereby consent to the use of photos of my eyes in scientific publications, on condition that they remain anonymous and that there be no mention of my identity.
11. I understand that the results of this research may lead to commercial outcomes for the industrial partner, but that my participation in the data collection does not entitle me to receive any financial benefits resulting from it.

(Please mark your choice) Yes ❑ No ❑

Consent to share my contact information

I hereby authorize the research team to contact me by email for the purpose of communicating their research results.

(Please mark your choice) Yes ❑ _____ No ❑

Email (please print)

Participant's first and last name
(Please print)

Participant's signature

Date :

Commitment of the research team

I confirm that I or my representative have explained to the aforementioned person the nature of their participation in this research activity, have asked them if they had any questions, and have answered their questions. We have made it clear that they will remain free to participate or to withdraw their participation at any time, by simple verbal notice. I, along with the research team, hereby undertake to respect the terms and conditions described in the present information and consent form and declare that I have provided a signed version of this document to the participant.

Lama Séoud (Please print)	Researcher's signature Date :
Doha Zrouki / Philippe Baumstimler (Please print)	Student's signature Date :